POLARIZATION EFFECTS OF NITRIC OXIDE PURE ROTATIONAL TRANSITIONS DEMONSTRATED BY COHERENT ANTI-STOKES RAMAN SCATTERING

by

Michael T. Arendt

A Thesis

Submitted to the Faculty of Purdue University

In Partial Fulfillment of the Requirements for the degree of

Master of Science in Mechanical Engineering

School of Mechanical Engineering

West Lafayette, Indiana

August 2019

THE PURDUE UNIVERSITY GRADUATE SCHOOL
STATEMENT OF COMMITTEE APPROVAL

Dr. Robert P. Lucht, Chair

School of Mechanical Engineering, School of Aeronautics and Astronautics

Dr. Carson Slabaugh

School of Aeronautics and Astronautics

Dr. Christopher Goldenstein

School of Mechanical Engineering

Approved by:

Dr. Jay Gore

Head of the Graduate Program

Dedicated to my parents.

ACKNOWLEDGMENTS

I would like to thank both Dr. Robert P. Lucht and Dr. Aman Satija for their outstanding expertise and knowledge on the topics presented in this thesis. Their guidance and patience have provided me the ability to learn and grow in a cutting-edge research environment of which I am most grateful.

TABLE OF CONTENTS

LIST OF TABLES 6
LIST OF FIGURES 7
ABSTRACT 9
1. INTRODUCTION 10
1.1 Motivation 10
1.2 CARS Theory 12
1.3 Polarization suppression theory in pure rotational and vibrational CARS 15
2. LITERATURE REVIEW 21
2.1 Nitric Oxide Spectroscopy 21
2.2 Pure Rotational Coherent Anti-Stokes Raman Scattering Spectroscopy 23
2.3 Dual-Pump Coherent Anti-Stokes Raman Scattering Spectroscopy 24
3. THEORY OF NITRIC OXIDE PURE ROTATIONAL TRANSITIONS 27
3.1 Overview and Term Definitions 27
3.2 Space-fixed Tensor Elements and Raman Transitions for a $^2\Pi$ Electronic Level 28
3.3 CARS Susceptibility, Rotational Transitions and Electronic Raman Transitions 31
4. DUAL-BROADBAND PRCARS OF NITRIC OXIDE 36
4.1 Dual-Broadband PRCARS Experimental System 36
4.2 DBB PRCARS Results and Analysis 37
5. DUAL-PUMP CARS OF NITRIC OXIDE 45
5.1 Dual-Pump CARS Experimental System 45
5.2 Polarization suppression of Nitrogen rotational and vibrational transitions 46
5.3 Raman polarizability tensor elements and effect of the non-resonant background 51
5.4 Dual-Pump CARS system analysis of nitric oxide 52
6. CONCLUSIONS 63
6.1 Summary 63
6.2 Future Work 64
REFERENCES 67

LIST OF TABLES

Table 1: Definition of Terms used for Theory of Nitric Oxide Pure Rotational Transitions 27

Table 2: Resonant CARS polarization angle at varying depolarization ratios 49

LIST OF FIGURES

Figure 1.1: CARS four-wave mixing process 19

Figure 1.2: Folded BOXCARS phase matching condition 19

Figure 1.3: Non-resonant four-wave mixing process 20

Figure 4.1: Dual-Broadband Pure Rotational CARS system optical layout 40

Figure 4.2: Dual-Broadband PRCARS energy level diagram 41

Figure 4.3: Transitions for O, P, Q, R, and S branches of NO 42

Figure 4.4: Comparison between experiment and theory from CARSFT code for N_2 pure rotational transitions 43

Figure 4.5: Nitric Oxide spectrum measured by the DBB-PRCARS system [34] 43

Figure 4.6: Closer look at the location of the electronic Raman transitions for NO at 120 cm^{-1} feature 44

Figure 4.7: Closer look at R branch transitions for NO that occur less than 20 cm^{-1} 44

Figure 5.1: Dual-Pump Combined CARS System optical layout 54

Figure 5.2: Polarization diagram of pump, probe, Stokes, and resonant CARS signal for polarization suppression of the rotational transitions of N_2 55

Figure 5.3: Energy level diagram for simultaneous acquisition of rotational and vibrational spectrum 56

Figure 5.4: Comparison between experiment and theory from CARSFT code for simultaneous acquisition of vibrational and rotational branches of N_2 57

Figure 5.5: Polarization suppression of N_2 rotational and vibrational levels by keeping Stokes beam constant and varying analyzer angle experimental data 57

Figure 5.6: Polarization suppression of N_2 rotational and vibrational levels by keeping Stokes beam constant and varying analyzer angle CARSFT theory 58

Figure 5.7: Polarization suppression of rotational S branch transitions of N_2 58

Figure 5.8: Variation of alpha term $\langle \eta v | \hat{\alpha}_{q=2}^{k=2} | \eta v \rangle^2$ in NO spectral simulation while holding all other terms constant 59

Figure 5.9: Variation of gamma term (γ_0^2) in NO spectral simulation while holding all other variables constant 59

Figure 5.10: Variation of non-resonant term (σ) in NO spectral simulation while holding all other terms constant 60

Figure 5.11: The rotational spectrum of NO with Stokes beam at 62° and the analyzer at 0° 61

Figure 5.12: The rotational spectrum of NO with Stokes beam at 62° and the analyzer at -52°.. 61

Figure 5.13: Comparison between NO spectral simulation and experimental results when the Stokes beam is 62° and the analyzer is 0° 62

Figure 6.1: Spectral simulation of NO at varying temperatures from 100 K to 300 K 65

Figure 6.2: Closer look at lower J level S branch transitions of spectral simulation at varying temperatures from 100 K to 300 K 66

Figure 6.3: Closer look around the 120 cm^{-1} Q branch transitions of spectral simulation at varying temperatures from 100 K to 300 K 66

ABSTRACT

Author: Arendt, Michael, T. MSME
Institution: Purdue University
Degree Received: August 2019
Title: Polarization Effects of Nitric Oxide Pure Rotational Transitions Demonstrated by Coherent Anti-Stokes Raman Scattering
Committee Chair: Robert P. Lucht

Dual-broadband and dual-pump nanosecond CARS experiments were performed to investigate the pure rotational transitions of the nitric oxide molecule. The former experiment was initially utilized to determine the pure rotational structure while the latter focused on polarization suppression of the pure rotational transitions of nitric oxide. A polarization calculation and analysis were conducted on the rotational and vibrational transitions of nitrogen, and the pure rotational transitions of nitric oxide were subjected to a similar polarization scheme. The electronic transitions that arise due to the spin-split nature of nitric oxide ground electronic energy levels were suppressed by the polarization scheme in a similar manner to the rotational S branch transitions. Results have been compared with a spectral simulation developed by Dr. Lucht, and the theory is partially presented. Comparison between simulation and experimental data yielded favorable agreement for the pure rotational transitions of nitric oxide.

1. INTRODUCTION

1.1 Motivation

Nitric Oxide (NO) is a fascinating molecule that captures the essence of a double-edged sword in its incredible utility mixed with dangerous toxicity. The nature of this radical molecule is the result of an unpaired valence electron allowing NO to be highly reactive. This ability to easily react with other molecules enables nitric oxide to transmit signals between mammalian cells, regulate blood pressure, defend against microbes and dilate blood vessels. On the other hand, NO plays a role in destroying the ozone layer of the Earth's atmosphere and can form nitric acid in acid rain [1]. One of the main methods in which nitric oxide is produced is through an endothermic reaction that occurs between nitrogen and oxygen at temperatures exceeding 2000 Kelvin. Since there is an excess of air in several types of combustion engines along with high temperatures, NO is often a concern with regards to emissions. Whether one is looking through the magnifying lens to determine how NO regulates functions in the human body or impacts the Earth's atmosphere, it has become increasingly clear that there is a strong need to understand the lasting effects of nitric oxide.

The science of combustion has been a field of increasing interest as fossil fuels have been overwhelmingly responsible for meeting the energy demands that propel modern economies and personal luxuries. As with most sciences, there are several methods to quantify this phenomenon of thermodynamics, chemistry and fluid dynamics in order to develop a more effective and efficient manner of providing energy. One method of describing a combustive environment is through the use of physical probes such as thermocouples and pressure transducers. However, these particular instruments have difficulty accurately describing the extreme temperatures and pressures of the combustive environment. Not only is it difficult for the physical probe to

mechanically withstand temperatures exceeding 2000 K and pressures above 10 atmospheres, but the nature of the device perturbs the thermodynamic properties and flow field in the region where measurements are taken. In order to achieve better accuracy, researchers have turned towards laser-based techniques that do not have the same limitations as physical probes.

As most laser-based methods only affect the matter within the combustive environment, laser-based techniques are considered non-invasive and non-intrusive compared to physical probes. Matter consists of atoms and molecules that have specific energy levels associated with its motion acting as a universal fingerprint for definitive identification. A molecule has the ability to store energy through four main modes by the means of translation, rotation, vibration and electronic states. Lasers are able to provide a monochromatic and coherent source of electromagnetic radiation to excite the energy modes of matter resulting in absorption, fluorescence, and scattering of radiation such that a signal is generated by this interaction. By analyzing these signals, scientists are capable of understanding flow fields through velocimetry techniques, species concentration through absorption and fluorescent techniques, and temperature measurements through coherent scattering techniques. One of these scattering techniques is called Coherent anti-Stokes Raman Scattering (CARS) and it is capable of achieving temperature and species measurements with excellent accuracy.

The CARS process can be briefly described as two laser beams creating a coherence amongst a molecule's energy mode transitions. A third laser beam is introduced so that the coherence is probed, and a CARS signal is generated due to conservation of energy and conservation of momentum. The shape of the spectrum indicates the temperature as it depicts which transitions are resonating in the CARS process. It is also important to note that the generated CARS signal is a laser beam with definitive propagation direction and polarization.

The polarization of the CARS signal can lead to clever methods of suppressing the non-resonant background signal that is inadvertently generated in the CARS process. CARS is also similar to another laser diagnostic technique called Raman scattering, which is the inelastic scattering of electromagnetic radiation when molecules are excited by a laser beam. Unlike CARS, Raman scattering does not have a definite propagation direction of the generated signal, but both techniques obey similar physics regarding their dipole moments. Understanding the effect of polarization on the scattering process is essential to interpreting the underlying quantum mechanical nature of the laser's interaction with a species of interest. A theoretical model may then be correlated with experimental data to determine a predictive model of that species and can be translated to other experiments to achieve accurate measurements.

The remainder of the introduction is dedicated to the theory of CARS spectroscopy and the theory of polarization effects on the CARS signal. The second chapter is a literature review on the spectroscopy of nitric oxide, pure rotational CARS experiments, and dual-pump CARS experiments. The third chapter discusses the theoretical calculations for the pure rotational and electronic transitions which has been developed by Dr. Lucht and will be presented in a different paper. The fourth chapter discusses the development and results obtained by a dual-broadband pure rotational CARS experiment for nitric oxide. The fifth chapter discusses the development of a dual-pump CARS system, a calculation on the polarization scheme, an overview of the parameters used in the CARS spectral simulation developed by Dr. Lucht, and the experimental results compared to theory for nitric oxide.

1.2 CARS Theory

Coherent Anti-Stokes Raman Scattering (CARS) is a four-wave mixing process driven by three laser beams that are overlapped in both time and space. A Raman coherence arises from the

difference between two of the three laser beams which are called the pump and Stokes beam. This coherence is often selected to match rotational or vibrational energy levels of interest for a given species. The probe beam is the third incident laser beam which scatters from the Raman coherence and creates a coherent, laser-like signal of the CARS beam. This four-wave mixing process must satisfy conservation of energy as two photons are destroyed while two photons are created. The equations and figures in the remainder of this section are discussed in further detail in Prof. Lucht's class notes [2], Eckbreth's book on laser diagnostics [3] and in Dr. Satija's Ph.D. dissertation [4].

The CARS process is shown in Figure 1.1 for a vibrational Raman coherence with conservation of energy being satisfied in the following equation.

$$\omega_3 = \omega_0 + \omega_1 - \omega_2 \tag{1.1}$$

The subscripts 0, 1, 2 and 3 correspond to the pump, probe, Stokes and CARS signal beams. The CARS signal beam will also have a definite propagation direction, $\vec{k}$, which is determined by conservation of momentum. The propagation vectors for each vector may be summed in the following equation

$$\vec{k}_3 = \vec{k}_0 + \vec{k}_1 - \vec{k}_2 \tag{1.2}$$

where the magnitude of each vector is determined by

$$|\vec{k}| = \frac{\eta\omega}{c} \tag{1.3}$$

In equation 1.3, η is the refractive index and c is the speed of light. By satisfying both conservation of energy and conservation of momentum, the process has correctly met the "phase matching condition" as the CARS mixing process is a parametric process. Collinear and planar phase matching conditions have been performed in literature, but folded BOXCARS has the best

spatial resolution and separation of laser beams [5]. The phase matching condition for folded BOXCARS is shown in Figure 1.2.

Since the pump, probe, Stokes and CARS signal beams are all laser beams, there is a relationship between the intensity of the CARS signal and the polarization of the laser beams. If all of the beams are polarized in parallel, then the CARS signal intensity is determined in the Eq 1.4. It is noted that ε_0 is the permittivity of the medium, $E(\omega_3)$ is the electric field of the CARS Signal, I is the intensity for each of the incident laser beams, $\chi_3(\omega_1, \omega_2)$ is the susceptibility of the CARS signal, and l is the length in which the laser beams interact.

$$I_3 = \frac{1}{2} c\varepsilon_0 |E(\omega_3)|^2 = \frac{\omega_3}{c^4 \varepsilon_0^4} I_0 I_1 I_2 |\chi_3(\omega_1, \omega_2)|^2 l^2. \tag{1.4}$$

The CARS susceptibility consists of both the resonant and non-resonant susceptibilities as shown in Eq. 1.5. The Raman linestrength is given as K_j, the dephasing Raman linewidth is Γ_j, $\Delta\omega_j$ is the detuning for a Raman transition, and j is an integer that represents a rotational transition. The Raman linewidth is determined by the thermodynamic conditions of the colliding species.

$$\chi_3(\omega_1, \omega_2) = \sum_j \left(K_j \frac{\Gamma_j}{2\Delta\omega_j - i\Gamma_j} \right) + \chi_{nr} \tag{1.5}$$

The linestrength is directly proportional to the Raman cross-section, $\left(\frac{\partial\sigma}{\partial\Omega}\right)$, which is dependent upon the substance that is scattered. The refractive index of the medium, η, is assumed to be one for both η_{refr1} and η_{refr2} since it is a gaseous medium. The subscript g denotes the ground state and the subscript e represents the excited state for the population density, n, and the level degeneracy, g. It is important to note that the population density and energy level degeneracy correspond to the temperature dependent statistical population distribution. More detailed

information regarding the statistical population distribution of a molecule can be found in Laurendau's book on statistical thermodynamics [6].

$$K_j = \frac{(4\pi)^2 \eta_{refr1} \varepsilon_0 c^4 \left(n_g - \frac{g_g}{g_e} n_e\right)_j}{\eta_{refr2} \hbar \omega_2^4 \Gamma_j} \left(\frac{\partial \sigma}{\partial \Omega}\right)_j \tag{1.6}$$

A closer look into the detuning parameter, $\Delta\omega_j$, reflects the difference between energy levels of rotational transitions.

$$\Delta\omega_j = \omega_j - (\omega_1 - \omega_2) = \frac{\left(\varepsilon_e - \varepsilon_g\right)_j}{\hbar} - (\omega_1 - \omega_2) \tag{1.7}$$

The last term in the CARS susceptibility equation is the non-resonant susceptibility that arises due to the four-wave mixing process, which is shown in Figure 1.3. The non-resonant susceptibility is a result of the medium's real, positive electronic response σ, and the relationship is illustrated in the equation below.

$$\chi_{nr} = \frac{3}{8}\sigma \tag{1.8}$$

1.3 Polarization suppression theory in pure rotational and vibrational CARS

Since the laser beams in the CARS mixing process can have a definite polarization, it is possible to suppress the resonant or non-resonant signal. This is particularly desirable as the non-resonant background can often interfere with the resonant CARS signal. It is possible to separate the resonant and non-resonant signals through adjusting the polarization of the pump, probe and Stokes beam before the mixing process occurs. An analyzer may then be placed in the path of the generated CARS signal beam at an angle capable of rejecting the non-resonant signal while still letting the resonant signal pass through it. This suppression does come at a fractional cost of the total CARS signal, and it may not be the best choice of action for applications that require a high signal-to-noise ratio. The following theory has been demonstrated by Lucht et al. [7] for the

rotational transition lines of N_2, and more detail can be found in Prof. Lucht's class notes [2]. This theory can also be applied to other molecules with a $^1\Sigma$ ground electronic state, and it begins with the compact equation to determine the amplitude of the CARS electric field $\vec{E}(\omega_3)$.

$$\vec{E}(\omega_3) = \frac{3i\omega_3}{2c}\Big[\chi^{(3)}_{1122}\hat{e}_0(\hat{e}_1 \cdot \hat{e}_2) + \chi^{(3)}_{1212}\hat{e}_1(\hat{e}_0 \cdot \hat{e}_2) + \chi^{(3)}_{1221}\hat{e}_2(\hat{e}_0 \cdot \hat{e}_1)\Big]E(\omega_0)E(\omega_1)E^*(\omega_2)l \tag{1.9}$$

The CARS electric field is dependent upon the orientation of the electric fields of the pump $\hat{e}_0$, probe $\hat{e}_1$ and Stokes $\hat{e}_2$ beams along with their respective components of the susceptibility tensor. The tensor components may be simplified by the following set of equations by assuming that the medium is isotropic with an absence of electronic resonance effects.

$$\chi^{(3)}_{1122} = \frac{1}{24}[\sigma + b(\omega_0 - \omega_2) + 2a(\omega_1 - \omega_2)] \tag{1.10}$$

$$\chi^{(3)}_{1212} = \frac{1}{24}[\sigma + 2a(\omega_0 - \omega_2) + b(\omega_1 - \omega_2)] \tag{1.11}$$

$$\chi^{(3)}_{1221} = \frac{1}{24}[\sigma + b(\omega_0 - \omega_2) + b(\omega_1 - \omega_2)] \tag{1.12}$$

The non-resonant signal arises from the electronic response of the medium σ, and the resonant signal is a result of the Raman contributions denoted as the a and b terms. The pure rotational Raman contribution is dependent on the invariant γ, which is considered the anisotropy of the molecule. The Placzek-Teller coefficient $b_{J'J}$ is dependent upon the total angular momentum quantum number J, and the expression for the S branch transitions is given below. More Placzek-Teller coefficients have been utilized by Penney et al. [8] for the Q branch and O branch transitions. The detuning parameter $\Delta\omega_{j0}$ is the difference between the Raman transition and the difference of the laser beams frequencies.

$$a(\omega_0 - \omega_2) = \beta_{JJ'}\left[-\frac{2}{45}b_{J'J}(\gamma)^2\right] \tag{1.13}$$

$$b(\omega_0 - \omega_2) = \beta_{JJ'}\left[\frac{2}{15}b_{J'J}(\gamma)^2\right] \tag{1.14}$$

$$\beta_{JJ'} = \frac{1}{\hbar\varepsilon_0}\left[n_J - \frac{2J+1}{2J'+1}n_{J'}\right]\frac{1}{2\Delta\omega_{j0} - i\Gamma_J} \tag{1.15}$$

$$b_{J'J} = b_{J+2,J} = \frac{3(J+1)(J+2)}{2(2J+1)(2J+3)} \tag{1.16}$$

$$\Delta\omega_{j0} = \omega_j - (\omega_0 - \omega_2) \tag{1.17}$$

The determination of $a(\omega_1 - \omega_2)$ and $b(\omega_1 - \omega_2)$ is similar to Eqs. 1.13 – 1.17 except the $\Delta\omega_{J0}$ term is replaced by the following equation.

$$\Delta\omega_{j1} = \omega_j - (\omega_1 - \omega_2) \tag{1.18}$$

If it is more desirable to calculate a vibrational transition, then Eq. 1.13-1.15 become the following equations for rovibrational transitions while the $\Delta\omega_{J0}$ and $\Delta\omega_{J1}$ remain the same. The remaining undefined terms are the Raman invariants of the polarizability tensor a' and γ', the Kronecker Delta function $\delta_{JJ'}$, and m_{mol} which is the mass of the molecule. The Kronecker Delta is equal to one for Q branch transitions ($\Delta J = 0$) and equal to zero for all other cases.

$$a(\omega_0 - \omega_2) = \beta_{vJJ'}\left[(a')^2\delta_{JJ'} - \frac{2}{45}b_{J'J}(\gamma')^2\right] \tag{1.19}$$

$$b(\omega_0 - \omega_2) = \beta_{vJJ'}\left[\frac{2}{15}b_{J'J}(\gamma')^2\right] \tag{1.20}$$

$$\beta_{vJJ'} = \frac{(v+1)\left[n_{vJ} - \frac{2J+1}{2J'+1}n_{(v+1)J'}\right]}{m_{mol}\omega_j\varepsilon_0}\frac{1}{2\Delta\omega_{j0} - i\Gamma_j} \tag{1.21}$$

For Q branch transitions, the Placzek-Teller coefficient is defined in the following equation.

$$b_{J'J} = b_{J,J} = \frac{J(J+1)}{(2J-1)(2J+3)} \tag{1.22}$$

The electric field polarization for both the non-resonant and pure rotational resonant signal may be determined by the equations presented in this section, and section 5.2 provides the derivation of the polarization angles used in the Dual-Pump CARS experiment.

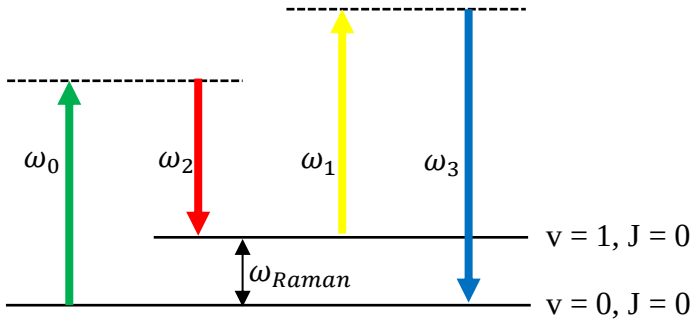

Figure 1.1: CARS four-wave mixing process

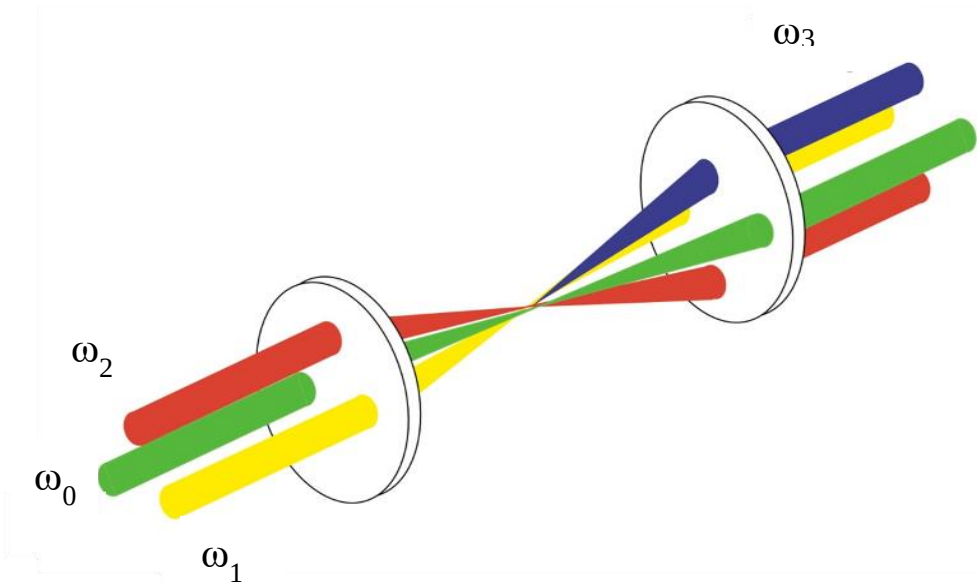

Figure 1.2: Folded BOXCARS phase matching condition

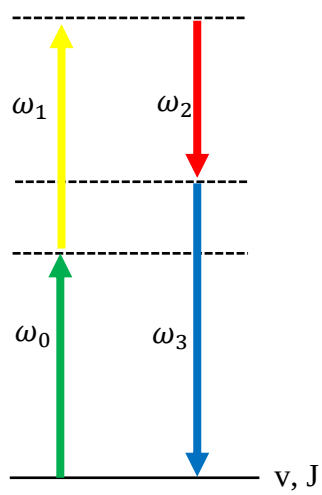

Figure 1.3: Non-resonant four-wave mixing process

2. LITERATURE REVIEW

2.1 Nitric Oxide Spectroscopy

Nitric oxide is an important molecule for spectroscopy as it is a stable diatomic molecule with a non-zero spin-split ground electronic level and orbital angular momentum. The non-zero angular momentum allows for lambda doubling, which occurs when the projection of the angular momentum vector along the internuclear axis can point towards either the nitrogen or oxygen atom. The spin splitting of the ground electronic level results in $^2\Pi_{1/2}$ and $^2\Pi_{3/2}$ components that are separated by 120 cm^{-1} and are of theoretical interest for the diatomic molecule. Nitric oxide is also an undesirable emission from the combustion process, and a better spectroscopic understanding of NO may lead to better combustion diagnostics.

The study of nitric oxide's Raman spectra begins nearly a century ago in 1930 when Rasetti [9] partially resolved its rotational spectrum by using a prism spectrograph with the exciting radiation at 253.7 nm. Rasetti also hinted at a significant feature at 120 cm^{-1} that may have occurred due to the spin-split nature of nitric oxide's ground electronic state. The Q branch electronic transitions between the $^2\Pi_{1/2}$ and $^2\Pi_{3/2}$ ground electronic states were then determined to result in a lifted baseline near 120 cm^{-1} by Renschler et al. [10] in 1969. Renschler also provided more resolution to the R branch and the S branch rotational structure of NO by using a helium neon laser at 633 nm. Renschler determined that the S branch is the strongest component of the rotational structure, and the R branch transitions decreases at an inversely proportional rate as the total angular momentum quantum number J increases. Fast et al. [11] was able to photograph the rotational Raman spectrum of nitric oxide with a spectral resolution around 0.3 cm^{-1} by using a mercury-vapor lamp with an excitation line at 435.8 nm. Fast et al. also depicted the O, P, Q, R and S branches of nitric oxide as stick spectrum obtained through theoretical

calculation. Fast et al. concluded that there is electrical component contribution of the Q branch that Rasseti initially suggested. The stick spectrum previously mentioned was developed by Lepard [12], and the literature included the basic theory in determining the rotational energy levels and wavefunctions for NO. Lepard concluded that the P, Q and R branches are weak in comparison to the rotational S branch of nitric oxide, which disagrees in the strength of these branches initially proposed by Rasetti. The aim of this thesis is to gain a better understanding of the behavior exhibited by the $^2\Pi$ electronic ground state in NO's spectrum.

While all of the previously mentioned works in literature have been focused on Raman scattering of the nitric oxide molecule, there have been more recent experiments which utilize CARS to measure the spectrum of NO. One of the first recordings of NO spectra using CARS occurred in 1981 by Beckmann et al. [13] and included the first vibrational band at a resolution of 0.05 cm^{-1}. This group also calculated the imaginary and real parts of the CARS signal and indicated the rotational structure spin splitting by observing the Q branch at high resolution. Doerk et al. [14] performed CARS rovibrational measurements on the first and second vibrational bands of NO gas at various temperatures and pressures by heating a ceramic cell with a tungsten coil. The group was capable of measuring concentrations of 0.25% NO mixed with N_2 at atmospheric pressure, and they unsuccessfully attempted to measure lower concentration levels through polarization suppression of the non-resonant background. To obtain a detection limit of 50 ppm, Kulatilaka et al. [15] performed electronic-resonance-enhanced coherent anti-Stokes Raman spectroscopy (ERE-CARS) on a H_2/air flame produced at atmospheric pressure by a Hencken Burner. The experiment consisted of a pump beam at 532 nm and a Stokes beam at 591 nm tuned to the Q branch $v" = 0 \rightarrow v' = 1$ transitions within the $X^2\Pi$ electronic level, and the probe beam at 236 nm was tuned to the $v" = 1 \rightarrow v' = 0$ vibrational band of the electronic

transition $A^2\Sigma^+$-$X^2\Pi$. Exciting the real electronic level as opposed to a virtual in traditional CARS, ERE-CARS is capable of obtaining a signal orders of magnitude stronger than conventional CARS. Chai et al. [16] demonstrated the utility of detecting NO in flames that have large temperature gradients, concentration gradients and soot through measuring a H_2/Air Hencken burner, a non-premixed H_2/Air counter-flow burner, and an Acetylene/Air Hencken burner by using ERE-CARS. It is important to note that there does not to appear to be any literature on pure rotational CARS of nitric oxide, which indicates the novelty of the experiments performed in this thesis.

2.2 Pure Rotational Coherent Anti-Stokes Raman Scattering Spectroscopy

There are several variations of taking CARS measurements. Perhaps the two most basic examples would be pure rotational CARS and vibrational CARS. The major difference between these two techniques is simply the energy levels which are excited during the CARS process. However, each technique may prove more useful in certain situations over another, and there are several instances where a combination of the two has yielded useful results. In general, pure rotational CARS has larger cross-sections and narrower linewidths than vibrational CARS. One distinct advantage for rotational CARS is its ability to measure multiple species simultaneously due to the rotational constant of most molecules being less than 20 cm^{-1}. On the other hand, a major disadvantage to rotational CARS is that the intensity decreases dramatically at high temperatures [17].

Pure Rotational Coherent Anti-Stokes Raman Scattering (PRCARS) highlights the rotational transitions of diatomic molecules all within the same vibrational energy level. This technique wasn’t typically used for CARS measurements until Eckbreth and Anderson [18] demonstrated the capabilities of dual-broadband PRCARS. They split a broadband beam with a full-width-at-

half-maximum (FWHM) of approximately 350 cm^{-1} to act as both the pump and Stokes beam while a narrowband laser beam acted as the probe to complete the CARS process. Even though the pump and Stokes beams were at the same frequency, the large bandwidth allows for the excitation of the pure rotational transitions that typically occur at Raman shifts less than 200 cm^{-1}. It can be noted that the rotational spectrum of molecules is more sensitive at lower temperatures because the lower energy levels are less populated, and vibrational CARS is traditionally used for higher temperature measurements. Zheng et al. [19] determined that the upper limit on the rotational CARS signal of N_2 was around 2000 K with a standard deviation of 9% by comparing with the vibrational CARS spectrum and thermocouple measurements. Alden et al. [20] could implement dual-broadband rotational CARS as well as vibrational CARS by using the double-folded BOXCARS technique to obtain the spectrum of N_2 and O_2. Satija and Lucht [21] were capable of generating a PRCARS signal with only two beams by using a phase matching scheme designed to allow a singular broadband beam to act as both the pump and Stokes beam.

2.3 Dual-Pump Coherent Anti-Stokes Raman Scattering Spectroscopy

The Dual-Pump Coherent Anti-Stokes Raman Scattering technique accounts for the ability to use one set of incident laser beam frequencies to generate a CARS signal for multiple species. Up until the late 1980s, the CARS process was implemented in the measurement of only a single species. Eckbreth and Anderson [22] developed a complicated technique based on two separate broadband Stokes lasers along with a couple fixed frequency beams that is capable of exciting multiple species. Lucht [23] later developed a three laser CARS system capable of measuring the vibrational spectrum of both nitrogen and oxygen by using a tunable pump beam. He used a beam at 532 nm from a frequency doubled Nd:YAG laser, a tunable narrow-band dye laser at

555 nm, and a broadband dye laser at 607 nm. As described with the nomenclature discussed in section 1.2, the 555 nm beam acts as the pump beam, the 532 nm beam acts as the probe beam, and the 607 nm beam is the Stokes beam. For nitrogen, the 532 nm beam acts as the pump, the 555 nm beam acts as the probe, and the 607 nm is the Stokes beam in both cases. The result is that both of the generated anti-Stokes CARS beams occur at 491 nm, and the narrowband dye laser beam was tuned such that there was a small separation between species' spectrum. The oxygen and nitrogen Q branch transitions occur at 1556 cm^{-1} and 2330 cm^{-1} respectively, and the beams were selected such that both spectrums are distinctly separated while displayed together within a 60 cm^{-1} range of the anti-Stokes frequency. Lucht et al. [7] later used a dual-pump CARS system to simultaneous acquire the pure rotational and vibrational CARS signal of nitrogen in a similar manner, and this technique was also implemented in one of the experiments of this thesis to determine the polarization analysis of nitric oxide.

As the measurement of multiple species through dual-pump CARS has become available, there have been several notable applications of the system in several different types of combustion devices and combinations of species measured. Lucht et al. [24] also performed his dual-pump CARS technique with single shot measurements on a laminar flat-flame McKenna burner, a high-pressure gas cell filled with CO_2-N_2 mixtures, and exhaust from a swirl stabilized combustor. The focus of these experiments was to determine the accuracy of species mole fraction and temperature measurements of the CO_2-N_2 pair, and standard deviations of 10% and 2% of the mean 0.10 CO_2 and 200K were reported for the McKenna burner. The dual-pump system was adapted by Roy et al. [25] to perform triple-pump CARS using three narrowband pump beams and a broadband Stokes beam. Roy et al. [26] also demonstrated a dual-pump, dual-broadband CARS system capable of obtaining accurate species concentrations and temperature

measurements of a Hencken burner at temperatures below 1500 K through the rotational spectra of the N_2-O_2 pair while the rovibrational structure from the N_2-CO_2 pair provided accurate measurements at higher temperatures. The dual-broadband aspect of the experiment measured the N_2-O_2 pair while the dual-pump aspect measured the N_2-CO_2 pair.

3. THEORY OF NITRIC OXIDE PURE ROTATIONAL TRANSITIONS

3.1 Overview and Term Definitions

The content of this chapter has been developed by Dr. Lucht to generate a spectral simulation for nitric oxide that was used in chapter 5 of this thesis. A more detailed analysis will be published in a paper at a later date, and the primary goal of this chapter is to provide information of the parameters adjusted in the spectral simulation. Table 1 includes a list of terms that are used by the equations in this chapter.

Table 1: Definition of Terms used for Theory of Nitric Oxide Pure Rotational Transitions

Symbol	Definition	Symbol	Definition
F	Rotational Level	N	Rotational Quantum Number
v	Vibrational Quantum Number	S	Electron Spin
J	Total Angular Momentum	Σ	Projection of the electron spin on the internuclear axis
M	Projection of Total Angular Momentum on the Z-axis	Ω	Sum of projections on the internuclear axis ($\Lambda + \Sigma$)
η	Unspecified Quantum Numbers associated with the $^2\Pi$ electronic level	Λ	Projection of the electron orbital angular momentum on the internuclear axis
ω_0	Angular Frequency of the Laser (Raman Scattering)	E_z	Laser Electric Field Amplitude
c	Speed of Light	ε_0	Dielectric Permittivity
N_i	Number of molecules in level i in the Raman probe	γ_{BA}	Dephasing Rate
$\hbar$	Planck's Constant divided by 2π		

3.2 Space-fixed Tensor Elements and Raman Transitions for a $^2\Pi$ Electronic Level

The wavefuntions for nitric oxide's $^2\Pi$ ground electronic level are assumed to behave as an intermediate between Hund's case (a) and Hund's case (b) given by Zare [27] and by Brown and Carrington [28]. These wavefunctions are represented in the following equations, and the parameters a_J, b_J, c_J and d_J are the normalization parameters for the wavefuntions.

$$|F_1; v; JM; \pm\rangle = a_J\left|\,^2\Pi_{1/2}\,; \eta\Lambda; v; JM; \pm\right\rangle + b_J\left|\,^2\Pi_{3/2}\,; \eta\Lambda; v; JM; \pm\right\rangle \tag{3.1}$$

$$|F_2; v; JM; \pm\rangle = c_J\left|\,^2\Pi_{1/2}\,; \eta\Lambda; v; JM; \pm\right\rangle + d_J\left|\,^2\Pi_{3/2}\,; \eta\Lambda; v; JM; \pm\right\rangle \tag{3.2}$$

The quantum states in the $^2\Pi_{1/2}$ and $^2\Pi_{3/2}$ electronic levels with respect to Hund's case (a) are written in the following equations. It is important to note that $\Lambda = \pm 1,\ S = \frac{1}{2}\ , \Sigma = \mp\frac{1}{2}$, and $\Omega = \pm\frac{1}{2}$ for the $^2\Pi_{1/2}$ ground electronic state while $\Lambda = \pm 1,\ S = \frac{1}{2}\ , \Sigma = \pm\frac{1}{2}$, and $\Omega = \pm\frac{3}{2}$ for the $^2\Pi_{3/2}$ ground electronic state.

$$\left|\,^2\Pi_{1/2}\,; \eta\Lambda; v; JM; \pm\right\rangle = \frac{1}{\sqrt{2}}\left[\left|\eta 1; v; \frac{1}{2} - \frac{1}{2}; J\,\frac{1}{2}M\right\rangle \pm (-1)^{J-\frac{1}{2}}\left|\eta - 1; v; \frac{1}{2}\frac{1}{2}\,; J - \frac{1}{2}M\right\rangle\right] \tag{3.3}$$

$$\left|\,^2\Pi_{3/2}\,; \eta\Lambda; v; JM; \pm\right\rangle = \frac{1}{\sqrt{2}}\left[\left|\eta 1; v; \frac{1}{2}\frac{1}{2}; J\,\frac{3}{2}M\right\rangle \pm (-1)^{J-\frac{1}{2}}\left|\eta - 1; v; \frac{1}{2} - \frac{1}{2}\,; J - \frac{3}{2}M\right\rangle\right] \tag{3.4}$$

It appears that the nitric oxide molecule behaves similar to Hund's case (a) for low values of the total angular momentum and Hund's case (b) for high values of the total angular momentum. This can be a result of the spin uncoupling from the internuclear axis as the total angular momentum increases.

The following equations result from a detailed analysis of Raman transitions for $^2\Pi$ electronic levels for the space-fixed polarizability tensor elements. The first of the following

equations corresponds to the observed Rayleigh line while the second is with respect to transitions within a similar rotational level. It is important to note that subscripts with p correspond to the space-fixed reference frame while the q corresponds to the molecule-fixed reference frame. The purpose for switching between reference frames allows for the separation between the rotational, vibrational and electronic energies of the diatomic molecule. The polarizability tensor element $\langle \eta v_B | \hat{\alpha}^2_{q=0} | \eta v_A \rangle$ is responsible for the rotational Raman transitions, and this value can be determined for nitric oxide by comparing experimental data of its rotational structure with that of a well-known molecule such as nitrogen. The polarizability tensor element $\langle \eta v_B | \hat{\alpha}^2_{q=2} | \eta v_A \rangle$ is responsible for the electronic Raman transitions, which can be obtained by comparing experimental data with a ratio of the rotational and electronic Raman polarizability tensor elements. The 3j symbols are the matrices which appear in the following equations, and they are a short-hand notation that may be converted to a form that can be solved algebraically. Edmunds [29] discussed the calculation and has several tables readily available on how to calculate the 3j symbols that appear in this chapter.

$$\begin{aligned} \left|\alpha^0_{p=0}(A,B)\right|^2 &= \left|\sum_{M_a}\sum_{M_b} \alpha^0_{p=0}(a,b)\right|^2 \\ &= (2J_A+1)(2J_B+1) \\ &\times \langle \eta v_B | \hat{\alpha}^0_{q=0} | \eta v_A \rangle^2 \left[a_J a'_J \begin{pmatrix} J_A & J_B & 0 \\ \frac{1}{2} & -\frac{1}{2} & 0 \end{pmatrix} - b_J b'_J \begin{pmatrix} J_A & J_B & 0 \\ \frac{3}{2} & -\frac{3}{2} & 0 \end{pmatrix} \right]^2 \end{aligned} \tag{3.5}$$

$$\left|\alpha_p^2(A,B)\right|^2 = \left|\sum_{M_a}\sum_{M_b}\alpha_p^2(a,b)\right|^2$$

$$= \frac{(2J_A+1)(2J_B+1)}{5}$$

$$\times \left\{\langle\eta v_B|\hat{\alpha}_{q=0}^2|\eta v_A\rangle\left[a_J a_J'\begin{pmatrix} J_A & J_B & 2 \\ \frac{1}{2} & -\frac{1}{2} & 0\end{pmatrix} - b_J b_J'\begin{pmatrix} J_A & J_B & 2 \\ \frac{3}{2} & -\frac{3}{2} & 0\end{pmatrix}\right]\right. \tag{3.6}$$

$$\pm\langle\eta v_B|\hat{\alpha}_{q=2}^2|\eta v_A\rangle(-1)^{J_A-\frac{1}{2}}\left[-a_J b_J'\begin{pmatrix} J_A & J_B & 2 \\ -\frac{1}{2} & -\frac{3}{2} & 2\end{pmatrix}\right.$$

$$\left.\left.+\, b_J a_J'\begin{pmatrix} J_A & J_B & 2 \\ -\frac{3}{2} & -\frac{1}{2} & 2\end{pmatrix}\right]\right\}^2$$

For Raman transitions, the incident laser beam propagates along the Y-axis while linearly polarized along the Z-axis. The scattered Raman intensities are detected at perpendicular angles with respect to the laser beam propagation. The X-direction and Y-direction polarizations are given by the following equations [30].

$$I_{ZX}^{\Omega} = \frac{(\omega_0+\omega_{AB})^4 N_A}{32c^3\pi^2\varepsilon_0(2J_A+1)}\langle\alpha_{ZX}(A,B)\alpha_{ZX}^*(A,B)\rangle E_Z^2 \tag{3.7}$$

$$I_{ZY}^{\Omega} = \frac{(\omega_0+\omega_{AB})^4 N_A}{32c^3\pi^2\varepsilon_0(2J_A+1)}\langle\alpha_{ZY}(A,B)\alpha_{ZY}^*(A,B)\rangle E_Z^2 \tag{3.8}$$

The orientation averages for nitric oxide are determined through a detailed analysis and result in the following equation.

$$\langle\alpha_{ZX}\alpha_{ZX}^*\rangle = \langle\alpha_{ZY}\alpha_{ZY}^*\rangle = \frac{1}{2}\langle\alpha_{p=1}^2\alpha_{p=1}^{2*}\rangle \tag{3.9}$$

3.3 CARS Susceptibility, Rotational Transitions and Electronic Raman Transitions

The CARS electric field amplitude is presented earlier in chapter 1 and has been placed here with a slight change in subscripts to account for convenience of the reader. The subscripts 1, 2, 3 and 4 correspond to the pump, Stokes, probe and CARS signal beams.

$$\vec{E}(\omega_4) = \frac{3i\omega_4}{2c}\Big[\chi^{(3)}_{1122}\hat{e}_1(\hat{e}_2\cdot\hat{e}_3) + \chi^{(3)}_{1212}\hat{e}_2(\hat{e}_1\cdot\hat{e}_3) + \chi^{(3)}_{1221}\hat{e}_3(\hat{e}_1\cdot\hat{e}_2)\Big]E(\omega_1)E(\omega_3)E^*(\omega_2)l \tag{3.10}$$

The general expression for the components of the CARS susceptibility for a $^2\Pi$ electronic level is given by the following equations [31] [32].

$$\chi^{(3)}_{1122}(-\omega_4;\omega_1,-\omega_2,\omega_3) = \frac{1}{24\varepsilon_0\hbar}\sum_{ab}\left[\frac{N_A^{(0)}}{(2J_A+1)} - \frac{N_B^{(0)}}{(2J_B+1)}\right]\left\{\frac{\langle\alpha_{XY}(A,B)\alpha_{YX}(A,B)\rangle}{[\Omega_{BA}-(\omega_1-\omega_2)-i\gamma_{BA}]} + \frac{\langle\alpha_{XX}(A,B)\alpha_{YY}(A,B)\rangle}{[\Omega_{BA}-(\omega_3-\omega_2)-i\gamma_{BA}]}\right\} \tag{3.11}$$

$$\chi^{(3)}_{1212}(-\omega_4;\omega_1,-\omega_2,\omega_3) = \frac{1}{24\varepsilon_0\hbar}\sum_{ab}\left[\frac{N_A^{(0)}}{(2J_A+1)} - \frac{N_B^{(0)}}{(2J_B+1)}\right]\left\{\frac{\langle\alpha_{XY}(A,B)\alpha_{XY}(A,B)\rangle}{[\Omega_{BA}-(\omega_1-\omega_2)-i\gamma_{BA}]} + \frac{\langle\alpha_{XY}(A,B)\alpha_{YX}(A,B)\rangle}{[\Omega_{BA}-(\omega_3-\omega_2)-i\gamma_{BA}]}\right\} \tag{3.12}$$

$$\chi^{(3)}_{1221}(-\omega_4;\omega_1,-\omega_2,\omega_3) = \frac{1}{24\varepsilon_0\hbar}\sum_{ab}\left[\frac{N_A^{(0)}}{(2J_A+1)} - \frac{N_B^{(0)}}{(2J_B+1)}\right]\left\{\frac{\langle\alpha_{XX}(A,B)\alpha_{YY}(A,B)\rangle}{[\Omega_{BA}-(\omega_1-\omega_2)-i\gamma_{BA}]} + \frac{\langle\alpha_{XY}(A,B)\alpha_{YX}(A,B)\rangle}{[\Omega_{BA}-(\omega_3-\omega_2)-i\gamma_{BA}]}\right\} \tag{3.13}$$

The CARS susceptibility requires an orientation average over the product of polarizabilities since the molecules in the medium are not all in the same direction. This orientation average is dependent upon the polarizations on the incident laser beams, and the results of an analysis are displayed in the following equations for nitric oxide CARS transitions.

$$\langle \alpha_{XX}\alpha_{YY}\rangle = \frac{1}{3}\langle \alpha^{0}_{p=0}\alpha^{0*}_{p=0}\rangle - \frac{1}{3}\langle \alpha^{2}_{p=0}\alpha^{2*}_{p=0}\rangle \tag{3.14}$$

$$\langle \alpha_{XY}\alpha_{YX}\rangle = \langle \alpha_{XY}\alpha_{XY}\rangle = \frac{1}{2}\langle \alpha^{2}_{p=2}\alpha^{2*}_{p=2}\rangle \tag{3.15}$$

For pure rotational Raman and CARS transitions, $v_A = v_B = v$ for nitric oxide within the $^2\Pi$ ground electronic levels corresponding to the $F_1 \rightarrow F_1$ and $F_2 \rightarrow F_2$ transitions. For $F_1 \rightarrow F_1$ transitions, Eq. 3.5 and Eq. 3.6 can be substituted into Eq. 3.9 to get the following equation.

$$\begin{aligned}
\langle \alpha_{ZX}\alpha^{*}_{ZX}\rangle = \langle \alpha_{ZY}\alpha^{*}_{ZY}\rangle &= \frac{1}{2}\langle \alpha^{2}_{p=1}\alpha^{2*}_{p=1}\rangle \\
&= \frac{(2J_A+1)(2J_B+1)}{10}\Bigg\{\langle \eta v|\hat{\alpha}^{2}_{q=0}|\eta v\rangle\Bigg[a_J a'_J\begin{pmatrix} J_A & J_B & 2 \\ \frac{1}{2} & -\frac{1}{2} & 0\end{pmatrix} \\
&\quad - b_J b'_J\begin{pmatrix} J_A & J_B & 2 \\ \frac{3}{2} & -\frac{3}{2} & 0\end{pmatrix}\Bigg] \\
&\quad \pm \langle \eta v|\hat{\alpha}^{2}_{q=2}|\eta v\rangle(-1)^{J_A-\frac{1}{2}}\Bigg[-a_J b'_J\begin{pmatrix} J_A & J_B & 2 \\ -\frac{1}{2} & -\frac{3}{2} & 2\end{pmatrix} \\
&\quad + b_J a'_J\begin{pmatrix} J_A & J_B & 2 \\ -\frac{3}{2} & -\frac{1}{2} & 2\end{pmatrix}\Bigg]\Bigg\}^2
\end{aligned} \tag{3.16}$$

By following a similar substitution, Eq. 3.14 and Eq. 3.15 become the following respective equations.

$$\langle \alpha_{XX}\alpha_{YY}\rangle = \frac{1}{3}\langle \alpha^{0}_{p=0}\alpha^{0*}_{p=0}\rangle - \frac{1}{3}\langle \alpha^{2}_{p=0}\alpha^{2*}_{p=0}\rangle$$

$$= \frac{(2J_A+1)(2J_B+1)}{3}\langle \eta v|\hat{\alpha}^{0}_{q=0}|\eta v\rangle^2 \left[a_J a'_J \begin{pmatrix} J_A & J_B & 0 \\ \frac{1}{2} & -\frac{1}{2} & 0 \end{pmatrix}\right.$$

$$\left. - b_J b'_J \begin{pmatrix} J_A & J_B & 0 \\ \frac{3}{2} & -\frac{3}{2} & 0 \end{pmatrix}\right]^2$$

$$- \frac{(2J_A+1)(2J_B+1)}{15}\left\{\langle \eta v|\hat{\alpha}^{2}_{q=0}|\eta v\rangle \left[a_J a'_J \begin{pmatrix} J_A & J_B & 2 \\ \frac{1}{2} & -\frac{1}{2} & 0 \end{pmatrix}\right.\right. \tag{3.17}$$

$$\left. - b_J b'_J \begin{pmatrix} J_A & J_B & 2 \\ \frac{3}{2} & -\frac{3}{2} & 0 \end{pmatrix}\right]$$

$$\pm \langle \eta v|\hat{\alpha}^{2}_{q=2}|\eta v\rangle (-1)^{J_A-\frac{1}{2}}\left[-a_J b'_J \begin{pmatrix} J_A & J_B & 2 \\ -\frac{1}{2} & -\frac{3}{2} & 2 \end{pmatrix}\right.$$

$$\left.\left. + b_J a'_J \begin{pmatrix} J_A & J_B & 2 \\ -\frac{3}{2} & -\frac{1}{2} & 2 \end{pmatrix}\right]\right\}^2$$

$$\langle \alpha_{XY}\alpha_{YX}\rangle = \langle \alpha_{XY}\alpha_{XY}\rangle = \frac{1}{2}\langle \alpha^{2}_{p=2}\alpha^{2*}_{p=2}\rangle$$

$$= \frac{(2J_A+1)(2J_B+1)}{10}\left\{\langle \eta v|\hat{\alpha}^{2}_{q=0}|\eta v\rangle \left[a_J a'_J \begin{pmatrix} J_A & J_B & 2 \\ \frac{1}{2} & -\frac{1}{2} & 0 \end{pmatrix}\right.\right.$$

$$\left. - b_J b'_J \begin{pmatrix} J_A & J_B & 2 \\ \frac{3}{2} & -\frac{3}{2} & 0 \end{pmatrix}\right] \tag{3.18}$$

$$\pm \langle \eta v|\hat{\alpha}^{2}_{q=2}|\eta v\rangle (-1)^{J_A-\frac{1}{2}}\left[-a_J b'_J \begin{pmatrix} J_A & J_B & 2 \\ -\frac{1}{2} & -\frac{3}{2} & 2 \end{pmatrix}\right.$$

$$\left.\left. + b_J a'_J \begin{pmatrix} J_A & J_B & 2 \\ -\frac{3}{2} & -\frac{1}{2} & 2 \end{pmatrix}\right]\right\}^2$$

The $F_2 \rightarrow F_2$ transitions follow the same analysis in which the only necessary distinction in equations is that a_J, a_J', b_J and b_J' should be replaced with c_J, c_J', d_J and d_J' for different normalization parameters.

For the case in which $v_A = v_B = v$ while level A and level B are in the F_1 and F_2 energy levels respectively, the electronic Raman and CARS transitions can be described by the following equations. The first corresponds to the simplification of Eq. 3.5 by substituting in the proper normalization parameters and solving the 3j symbols. The normalization parameters result in a relation such that $c_j' = -b_J$ and $d_J' = a_J$, and this term is only non-zero if $J_A = J_B$. However, the term still becomes zero through the analysis of the 3j symbols as shown below.

$$\langle \alpha_p^0(A,B)\alpha_p^{0*}(A,B)\rangle$$

$$= (2J_A+1)^2 \langle \eta v | \hat{\alpha}_{q=0}^0 | \eta v \rangle^2 \left[-a_J b_J \frac{(-1)^{J_A-\frac{1}{2}}}{\sqrt{2J_A+1}} - b_J a_J \frac{(-1)^{J_A-\frac{1}{2}}}{\sqrt{2J_A+1}} \right]^2 = 0 \tag{3.19}$$

Eq. 3.6 can follow similar simplifications such that it reduces to the following equation.

$$\langle \alpha_p^2(A,B)\alpha_p^{2*}(A,B)\rangle = \left| \sum_{M_a} \sum_{M_b} \alpha_p^2(a,b) \right|^2$$

$$= \frac{(2J_A+1)(2J_B+1)}{5}$$

$$\times \left\{ \langle \eta v | \hat{\alpha}_{q=0}^2 | \eta v \rangle \left[a_J c_J' \begin{pmatrix} J_A & J_B & 2 \\ \frac{1}{2} & -\frac{1}{2} & 0 \end{pmatrix} - b_J d_J' \begin{pmatrix} J_A & J_B & 2 \\ \frac{3}{2} & -\frac{3}{2} & 0 \end{pmatrix} \right] \right. \tag{3.20}$$

$$\pm \langle \eta v | \hat{\alpha}_{q=2}^2 | \eta v \rangle (-1)^{J_A-\frac{1}{2}} \left[-a_J d_J' \begin{pmatrix} J_A & J_B & 2 \\ -\frac{1}{2} & -\frac{3}{2} & 2 \end{pmatrix} \right.$$

$$\left. \left. + b_J c_J' \begin{pmatrix} J_A & J_B & 2 \\ -\frac{3}{2} & -\frac{1}{2} & 2 \end{pmatrix} \right] \right\}^2$$

The equations highlighted in this chapter may be used to determine the pure rotational transitions for nitric oxide. It is important to note that selection rules allow for O, P, Q, R and S branch transitions of the NO diatomic molecule, and the 3j symbols should be calculated according to those transitions.

4. DUAL-BROADBAND PRCARS OF NITRIC OXIDE

4.1 Dual-Broadband PRCARS Experimental System

The Dual-Broadband Pure Rotational Coherent Anti-Stokes Scattering (DBB-PRCARS) technique consists of three laser beams to carry out the resonant four-wave mixing process and is shown in Figure 4.1. The Q-switched Nd:YAG (Spectra-Physics Model 290-10) laser utilizes its second harmonic output at 532 nm with a full-width-at-half-maximum (FWHM) bandwidth at 0.8 cm^{-1} to act as both the probe beam and to pump a custom broadband dye laser (BBDL). A solute of Sulforhodamine 640 is dissolved in a solvent of methanol to get an output centered at 607 nm with a FWHM bandwidth near 300 cm^{-1}. The concentrations used for the broadband dye laser is 40 mg/L and 15 mg/L for the oscillator and amplifier respectively. A beam splitter divides the output of the BBDL such that one beam becomes the pump laser beam and the other becomes the Stokes laser beam. The energies for the pump, probe and Stokes beams are each at 20 mJ/pulse for this experiment. The three beams incident on a plano-convex lens with a focal length of 250 mm can satisfy the folded BOXCARS phase matching condition. The convergence of the three laser beams occurs within a 1/4” Swagelok tee fitting, which dispenses the gaseous flow of the species of interest. The three incident laser beams and the generated CARS signal beam are directed onto another plano-convex lens to allow the beams to be parallel once again. The pump, Stokes, and probe beam are then dumped while the CARS signal beam passes a razor’s edge that blocks excess electromagnetic radiation from the probe beam. The PRCARS signal beam is directed into a 0.75-m spectrometer, where the spectrum is dispersed by a diffraction grating (1200 grooves/mm) and detected by a back-illuminated charge-coupled-device known as a CCD (Andor DV887ECS-BV).

As previously mentioned, the CARS mixing process for this experiment occurs within a 1/4” Swagelok tee fitting that dispenses the desired gases. The flow rate is determined by a needle valve upstream of the tee fitting. The smallest flow rate is determined by flowing a nontoxic, inert gas in order to maintain the desired conditions where only enough gas was present to saturate small probe volume. The gases which flowed out of the tee were immediately suctioned up a flexible ventilation line and into a fume hood that vents out of the roof of the building. To ensure safe operation of the experiment, a toxic gas detector (Enmet SPECTRUM ON-LINE) is strategically placed such that the operators may shut off the gas line immediately if the sensor detects any amount toxicity.

4.2 DBB PRCARS Results and Analysis

The PRCARS signal of nitrogen and nitric oxide were obtained at room temperature and atmospheric pressure. The energy level diagram of the pure rotational spectrum is illustrated in Figure 4.2 where the 607 nm beams act as both the pump and Stokes beams to create a resonance of the rotational levels over a broad range. Nitrogen spectra was first measured to determine the spectral dispersion of the DBB-PRCARS system. To obtain an accurate spectrum, several thousand shots were averaged for both this experimental system and the Dual-Pump CARS system discussed in the following chapter. The background data was obtained by blocking one of the three incident laser beams upstream of the CARS mixing process, and this background was subtracted from the raw data for nitrogen. The data was then divided by the non-resonant signal that was generated when argon gas was flowed through the probe volume. Since the CARS signal is proportional to the square of the number density, the square root is taken from the intensity counts. The Raman shift of nitrogen is well known which allows the pixel numbers of the CCD to be transformed to wavenumbers. The spectrum was then compared with a theoretical

fit obtained through the CARSFT code [33], and Figure 4.4 indicates that there is good agreement between experiment and theory. The process was then repeated for nitric oxide where the nitrogen spectrum essentially provided a calibration of the pixel to frequency transformation in determining the Raman shift for NO.

There are O, P, Q, R and S branch transitions that are of interest for nitric oxide, and Figure 4.3 depicts these transitions that occur amongst the $^2\Pi_{1/2}$ and $^2\Pi_{3/2}$ ground electronic states. The difference between the two ground electronic states is approximately 120 cm^{-1}, and it is possible for some transitions to occur between the two states. The O, P, Q, R and S branch each exhibit resonant transitions in which the change of the angular momentum quantum number ΔJ is equal to -2, -1, 0, 1 and 2 respectively. Since NO has a non-zero angular momentum in its ground electronic states, it is possible to have lambda doubling occur such that there are actually four ground electronic states where the projection of the angular momentum vector along the internuclear axis could point towards either the nitrogen atom or oxygen atom. However, the resolution of the experimental system is not high enough such that all of states become visible. The data obtained reflects how two of the ground electronic states produce pure rotational data with the goal of visualizing the strength of the transitions.

A mixture of 50% nitric oxide and 50% helium was used in the experiment to determine the PRCARS structure of NO. Since pure nitric oxide is an expensive gas, it made sense to combine a lower concentration of it with helium, which does not have a significant enough signal to interfere with the NO signal. The pure rotational spectrum averaged over thousands of shots is depicted in Figure 4.5 with the S branch transitions dominating most of the spectrum and the expected Q branch location occurring at 120 cm^{-1}. The spin splitting effects of the ground electronic state is evident first at 68 cm^{-1} and the gap between the $^2\Pi_{1/2}$ and $^2\Pi_{3/2}$ states becomes

more evident at higher Raman shifts. A closer look at the 120 cm^{-1} features shown in Figure 4.6 indicates that the Q branch transitions between spin-split ground electronic states appears to weak in nature. A strong indication of these Q branch transitions would have been a slight lift in the baseline of NO's spectrum. Another goal of this experiment would be able to identify the structure of the R branch transitions of NO. However, Figure 4.7 indicates that resolution of the system and the linewidth of the probe beam is too broad to distinctly see the transitions that occur at Raman shifts less than 20 cm^{-1} [34].

The next step in the process of understanding the pure rotational transitions of nitric oxide would be to adjust the polarization of the incident laser beams to suppress the S branch. This polarization suppression would allow for a theoretical understanding of how Q branch transitions between the spin split $^2\Pi_{1/2}$ and $^2\Pi_{3/2}$ are affected with respect to the S branch. The DBB-CARS system utilized in this section allows for uncertainty as to which of the laser beams correspond to the pump and Stokes beam. Therefore, it is necessary to switch to the Dual-Pump CARS system introduced in the next chapter. The dual-pump aspect will allow for the simultaneous acquisition of rotational and vibrational spectrum of nitrogen as demonstrated by Lucht et al. [7]. The dual-pump CARS system has distinct frequencies on the pump, probe and Stokes beams such that the polarization of each beam is known.

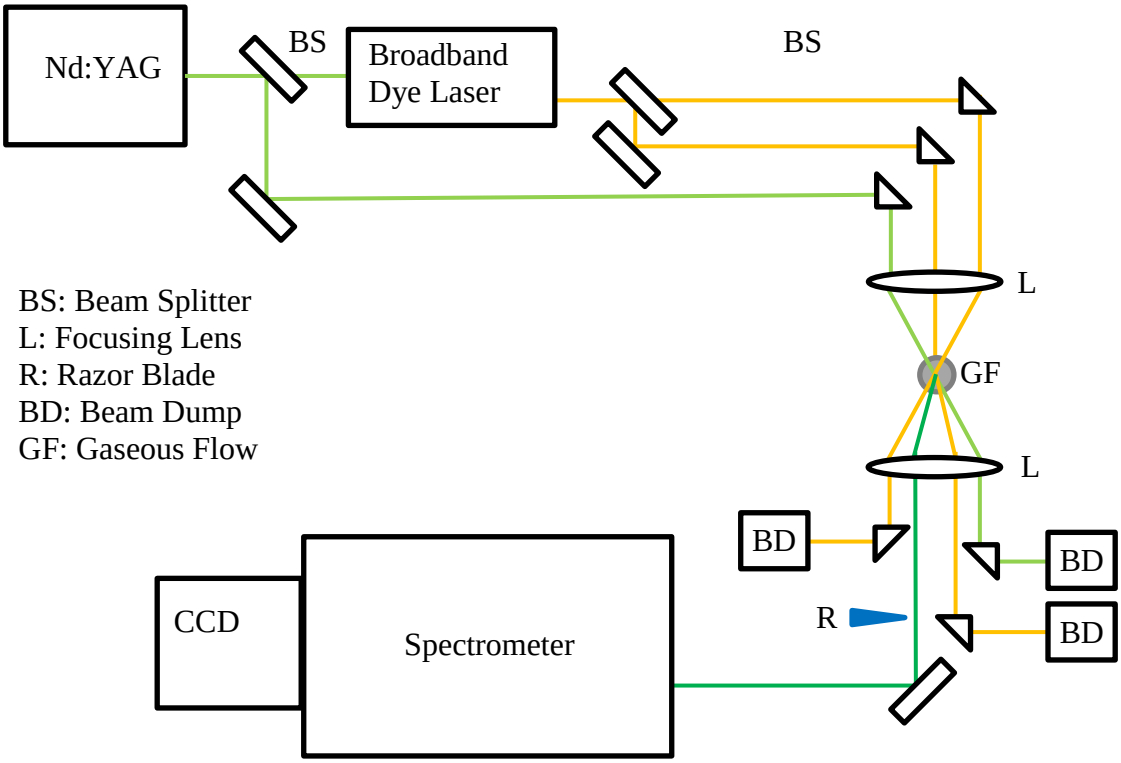

Figure 4.1: Dual-Broadband Pure Rotational CARS system optical layout

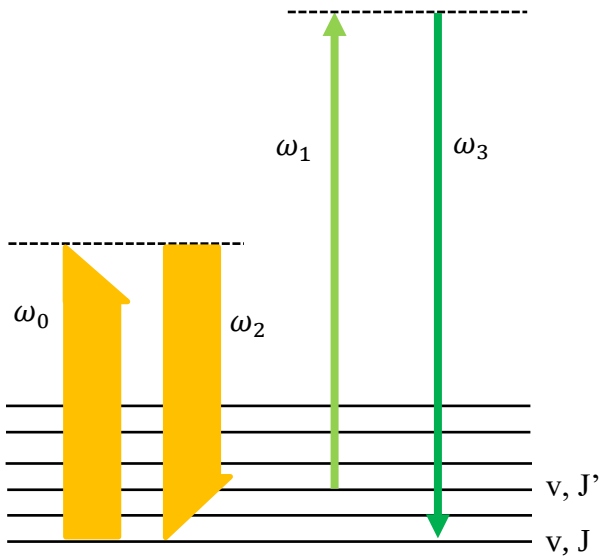

Figure 4.2: Dual-Broadband PRCARS energy level diagram

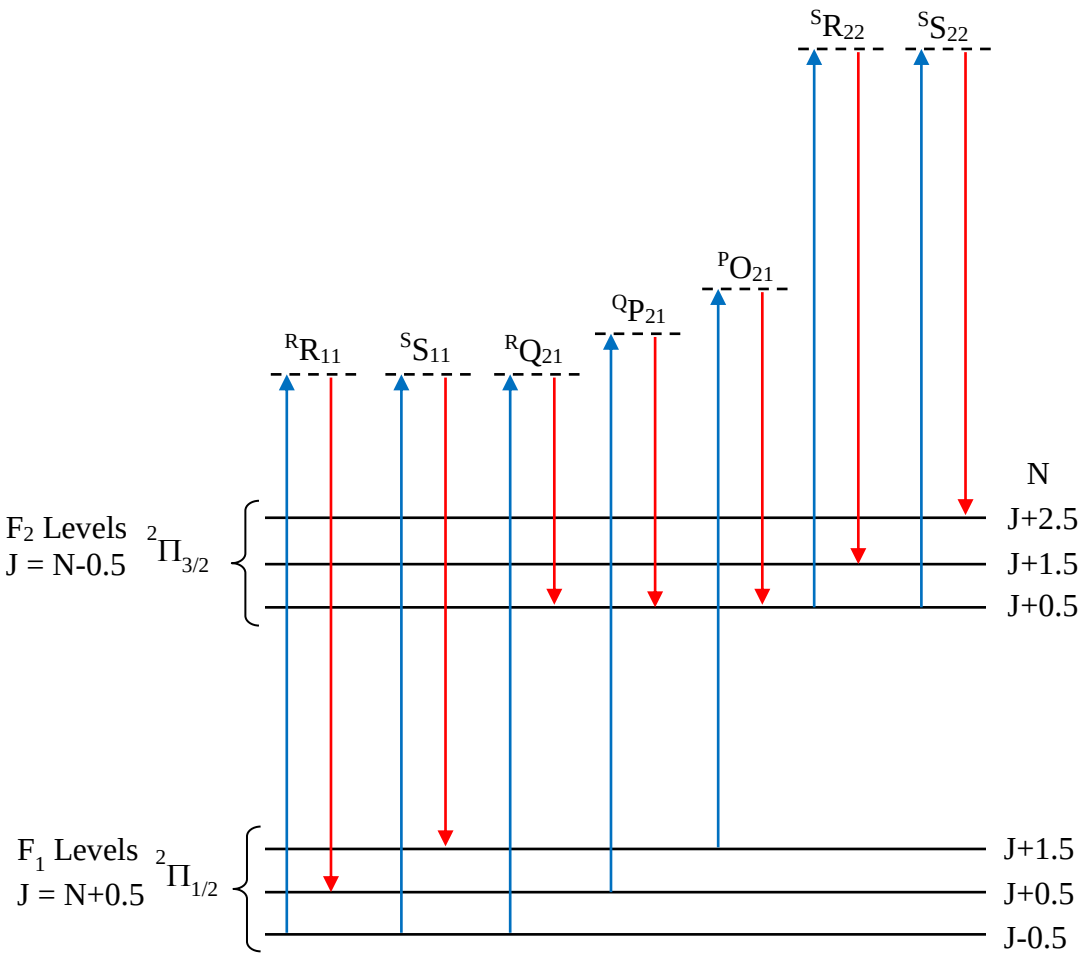

Figure 4.3: Transitions for O, P, Q, R, and S branches of NO

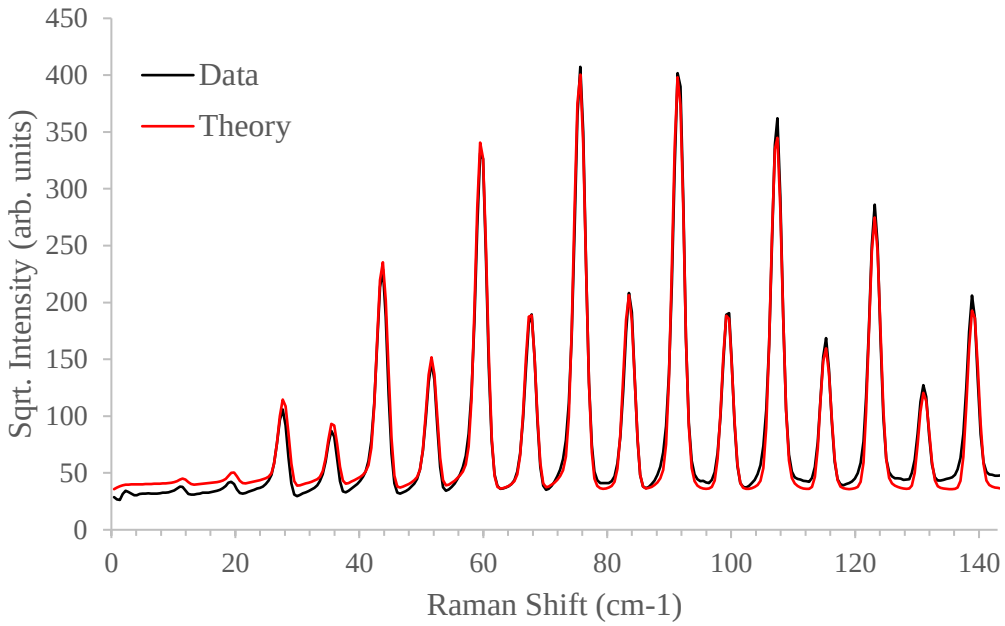

Figure 4.4: Comparison between experiment and theory from CARSFT code for N_2 pure rotational transitions

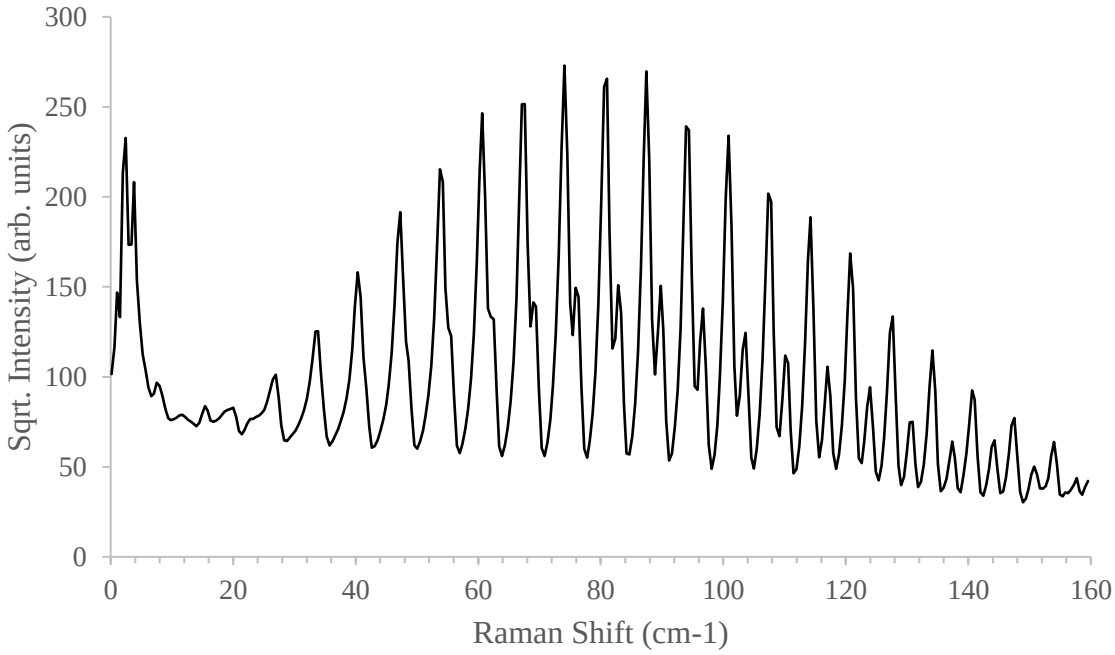

Figure 4.5: Nitric Oxide spectrum measured by the DBB-PRCARS system [34]

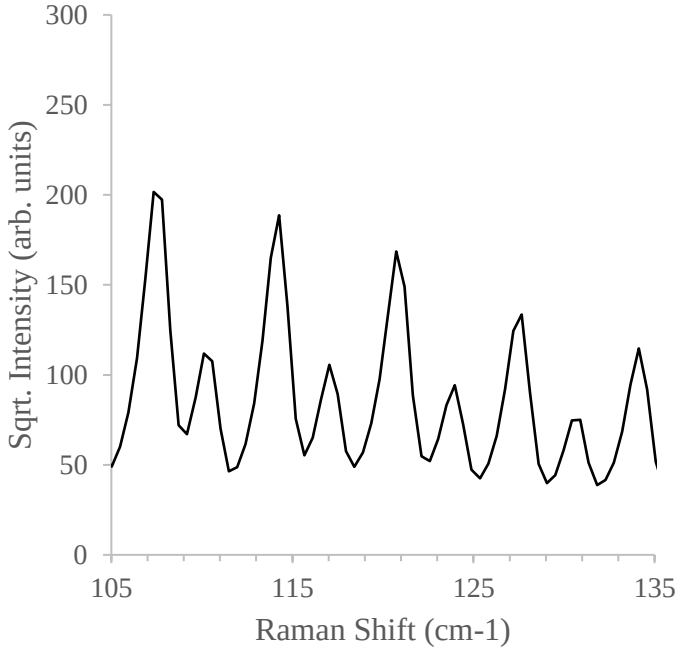

Figure 4.6: Closer look at the location of the electronic Raman transitions for NO at 120 cm^{-1} feature

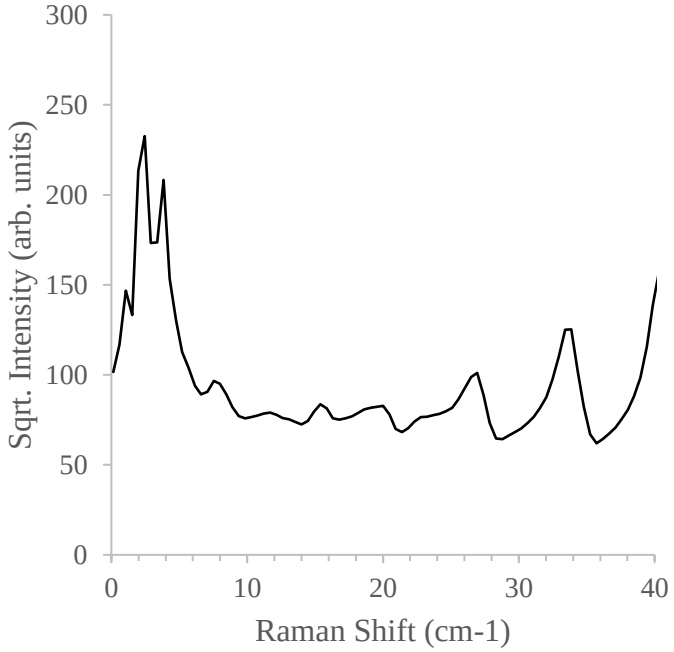

Figure 4.7: Closer look at R branch transitions for NO that occur less than 20 cm^{-1}

5. DUAL-PUMP CARS OF NITRIC OXIDE

5.1 Dual-Pump CARS Experimental System

Dual-Pump Coherent Anti-Stokes Raman Scattering is another three laser CARS system shown in Figure 5.1. The system begins with another Q-switched Nd:YAG laser utilizing its second harmonic output at 532 nm with FWHM around 0.8 cm^{-1}. This beam is split twice in order to pump both a narrow band dye laser (NBDL) and the same custom BBDL used in the previous experimental system. The NBDL (Continuum Model ND60) utilizes a solute mixture of Rhodamine 610 and Rhodamine 640 dissolved in methanol to get an output centered at 602 nm with FWHM around 0.1 cm^{-1}. The concentration used for the NBDL is 21.3 mg/L and 37.8 mg/L of rhodamine 610 and rhodamine 640 respectively for the oscillator, and the amplifier has a concentration of 10.6 mg/L and 18.7 gm/L of rhodamine 610 and rhodamine 640. The BBDL uses the same mixture of Sulforhodamine 640 and methanol with an output centered at 607 nm and a FWHM of 300 cm^{-1}. Polarizers are then placed in front of the 607 nm and 532 nm laser beams. These polarizers are responsible for ensuring that the polarizations are parallel to each other within the lab reference frame. There is an adjustable half-wave plate placed downstream of the 607 nm polarizer and upstream of the 250 mm plano-convex lens. This wave plate is used to rotate the polarization of the 607 nm beam. The energies for the 532 nm, 602 nm and 607 nm beams are 20, 10 and 30 mJ/pulse respectively. The beams pass through a 250 mm plano-convex lens and then converge within the same tee fitting previously mentioned in section 4.1. The method of administering gaseous flow was also described in that section. The beams are directed onto another 250 mm plano-convex lens, and all beams other than the CARS beam are dumped. The CARS beam passes through an analyzer, which may be set at different angles to match the desired conditions. The CARS signal beam is directed into the 0.75-m spectrometer, dispersed by

a diffraction grating with 1200 grooves/mm and detected by the same CCD previously used for the DBB-PRCARS system.

5.2 Polarization suppression of Nitrogen rotational and vibrational transitions

The dual-pump CARS system is designed to depict both the vibrational and rotational energy levels of nitrogen, which can then be related to the transitions of nitric oxide. The first vibrational transition of N_2 occurs at 2330 cm^{-1} while the BBDL can excite the rotational energy transitions within 200 cm^{-1}. The design of this system allows either the rotational (S branch) transitions or the vibrational (Q branch) transition of the nitrogen molecule to be suppressed when introduced to polarizers. Since the depolarization of nitric oxide is unknown, it is assumed that the transitions for nitric oxide behave in a similar manner to those of the nitrogen molecule.

Continuing with the polarization suppression theory of pure rotational transitions in section 1.3, the resonant and non-resonant polarization angles have been determined in the remainder of this section. The calculation starts with the following equation which determines the direction of CARS electric field.

$$\vec{E}(\omega_3) \propto \left[\chi^{(3)}_{1122}\hat{e}_0(\hat{e}_1 \cdot \hat{e}_2) + \chi^{(3)}_{1212}\hat{e}_1(\hat{e}_0 \cdot \hat{e}_2) + \chi^{(3)}_{1221}\hat{e}_2(\hat{e}_0 \cdot \hat{e}_1)\right] \tag{5.1}$$

Both the pump and probe beams have a polarization along the reference $\hat{x}$-axis and are denoted by $\hat{e}_0$ and $\hat{e}_1$ respectively. The Stokes beam is adjusted to an angle θ with respect to the $\hat{x}$-axis with a direction $\hat{e}_2$ and is shown in Figure 5.2.The dot product of the electric field directions of the laser beam is simplified and can be written as the following.

$$\vec{E}(\omega_3) \propto \left[\chi^{(3)}_{1122}\cos(\theta)\hat{e}_0 + \chi^{(3)}_{1212}\cos(\theta)\,\hat{e}_1 + \chi^{(3)}_{1221}\hat{e}_2\right] \tag{5.2}$$

It is assumed that the detuning parameter $\Delta\omega_{j0}$ and $\Delta\omega_{j1}$ are zero since the Raman contribution is only significant if it is close enough to each rotational transition. This also indicates that only

the terms $a(\omega_0 - \omega_2)$ and $b(\omega_0 - \omega_2)$ are close enough to the transitions to contribute to the susceptibility terms.

$$\chi^{(3)}_{1122} = \frac{1}{24}[\sigma + b(\omega_0 - \omega_2) + 2a(\omega_1 - \omega_2)] = \frac{1}{24}[\sigma + b] \tag{5.3}$$

$$\chi^{(3)}_{1212} = \frac{1}{24}[\sigma + 2a(\omega_0 - \omega_2) + b(\omega_1 - \omega_2)] = \frac{1}{24}[\sigma + 2a] \tag{5.4}$$

$$\chi^{(3)}_{1221} = \frac{1}{24}[\sigma + b(\omega_0 - \omega_2) + b(\omega_1 - \omega_2)] = \frac{1}{24}[\sigma + b] \tag{5.5}$$

Since the pump and probe beams have the same electric field direction, those terms may be combined into the electric field vector $\hat{e}_0$. Eqs. 5.3 - 5.5 may then be substituted into equation 5.2 to result in the following expression.

$$\vec{E}(\omega_3) \propto [\{2\sigma + 2a + b\}\cos(\theta)\hat{e}_0 + \{\sigma + b\}\hat{e}_2] \tag{5.6}$$

The vector field for the pump/probe beams can be written as $\hat{e}_0 = \hat{x}$, and the vector field of the Stokes beam is determined by $\hat{e}_2 = \cos(\theta)\,\hat{x} + \sin(\theta)\,\hat{y}$. Simplification of Eq. 5.6 yields the following results for the electric field vector of the CARS signal beam.

$$\vec{E}(\omega_3) \propto [\{3\sigma + 2a + 2b\}\cos(\theta)\hat{x} + \{\sigma + b\}\sin(\theta)\,\hat{y}] \tag{5.7}$$

The non-resonant electric field vector, $\hat{e}_{nr}$, is identified by the terms including the medium's electronic response σ, and the remainder of the terms represent the resonant electric field vector, $\hat{e}_{res}$, for the pure rotational transitions.

$$\hat{e}_{res} = \{2a + 2b\}\cos(\theta)\,\hat{x} + b\sin(\theta)\,\hat{y} \tag{5.8}$$

$$\hat{e}_{nr} = 3\cos(\theta)\,\hat{x} + \sin(\theta)\,\hat{y} \tag{5.9}$$

The angle with respect to the x-axis for each vector field can be determined by taking the inverse tangent of the y-component divided by the x-component.

$$\theta_{res} = \tan^{-1}\left(\frac{b\sin(\theta)}{\{2a + 2b\}\cos(\theta)}\right) \tag{5.10}$$

$$\theta_{nr} = \tan^{-1}\left(\frac{\sin(\theta)}{3\cos(\theta)}\right) \tag{5.11}$$

The depolarization ratio, which is the ratio of the perpendicular component of intensity with respect to the parallel component of intensity, can be written as the following equation [2].

$$\rho = \frac{b(\omega_0 - \omega_2)}{2a(\omega_0 - \omega_2) + 2b(\omega_0 - \omega_2)} = \frac{b(\omega_1 - \omega_2)}{2a(\omega_1 - \omega_2) + 2b(\omega_1 - \omega_2)} \tag{5.12}$$

Substituting Eq. 5.12 into Eq. 5.10 results in the following expression for θ_{res} with respect to the depolarization ratio and Stokes beam polarization angle.

$$\theta_{res} = \tan^{-1}\left(\frac{\rho\sin(\theta)}{\cos(\theta)}\right) \tag{5.13}$$

For pure rotational S branch transitions, the depolarization ratio is equivalent to 0.75 and Eq. 5.13 becomes only a function of the Stokes beam polarization angle. For vibrational Q branch transitions, the depolarization ratio can also be written as the following equation [2] where a' and γ' are the mean and anisotropy of the molecule.

$$\rho = \frac{3b_{J,J}(\gamma')^2}{45(a')^2 + 4b_{J,J}(\gamma')^2} \tag{5.14}$$

The value of $(a')^2$ and $(\gamma')^2$ are $1.515 \times 10^{-59}\ \left(\frac{C^4m^2}{J^2}\right)$ and $2.062 \times 10^{-59}\ \left(\frac{C^4m^2}{J^2}\right)$ respectively for nitrogen [2]. For high values of J for Q branch transitions, the value of the placzek-Teller coefficient $b_{J,J}$ tends towards a value of 0.25 and the depolarization ratio becomes 0.022 for vibrational transitions of N_2.The following table provides the polarization angle of the resonant CARS signal with respect to varying depolarization ratio for a set Stokes beam angle of 62°.

Table 2: Resonant CARS polarization angle at varying depolarization ratios

ρ	θ_{res}
0	0°
0.022	2.37°
0.05	5.37°
0.10	10.65°
0.20	20.61°
0.30	29.43°
0.40	36.95°
0.50	43.24°
0.60	48.45°
0.70	52.78°
0.75	54.67°
0.80	56.39°
0.90	59.43°
1	62°

To suppress either the resonant or non-resonant signal, an analyzer may be placed perpendicular to the corresponding electric field. It is important to note that suppressing a component of the CARS signal can be beneficial in achieving the desired effects, but the overall signal intensity will decrease as a whole and could lead to difficulty in recording the CARS signal for some applications.

The polarization suppression process described above has been conducted for nitrogen gas at room temperature and atmospheric pressure in order to match the experimental conditions. For a Stokes beam at an angle of 62°, the angle for the resonant pure rotational transitions occurs at 54.67°, and the analyzer may be placed at a perpendicular angle to reject the pure rotational structure of the CARS signal beam.

The initial set of data for N_2 was collected at a parallel polarization for all of the laser beams, and this data is fit with theory from the CARSFT code [33]. Figure 5.4 indicates that the system is calibrated and in good agreement with the CARSFT code. The rotational S branch transitions occur at Raman shifts less than 175 cm^{-1} whereas the vibrational transition

$v = 0 \rightarrow v = 1$ has a distinct peak at 180 cm^{-1} on the x-axis. The pump and probe beam frequencies were set such that both the rotational and vibrational spectrum of N_2 could be displayed on the CCD together even though difference between the two sets of transitions occurs thousands of wavenumbers apart. An energy level diagram illustrating the process for the simultaneous acquisition of rotational and vibrational spectra of N_2 is in Figure 5.3 and also demonstrated by Lucht et al. [7].The pump and probe beams remained parallel to each other while the Stokes beam was rotated such that the vibrational and rotational transitions for N_2 were distinctly separated in polarization. It was determined experimentally by observing the intensity of each of the two resonant CARS signals changing with respect to the angle of the Stokes beam, and it was recorded that 62° provided the largest difference. With the Stokes beam set to 62°, the analyzer was rotated at various angles to determine the best suppression case experimentally which occurred at an angle of -52° as shown in Figure 5.5. This didn't match the expected calculation performed earlier in this section as the analyzer transmission axis should have been placed perpendicular to the resonant angle of the pure rotational CARS signal, which would be an analyzer angle of -35°. This is responsible for a difference of 17° between the calculated analyzer transmission angle and experimental angle. Possible sources of error for this difference could be a result of error in determining the location of the analyzer with respect to incident beam orientations. There is also a range of approximately $\pm 5°$ for the locations in which the maximum and minimum locations of rotational and vibrational suppression. It was determined experimentally that the vibrational signal of N_2 was suppressed at -92° which differs by 4° with the calculation of the analyzer angle of -88°. Figure 5.6 is a theoretical calculation by CARSFT code of the N_2 spectrum at the same analyzer angles as Figure 5.5, and the simulations match the same trend but differ in the minimum which matches the calculations. Figure 5.7 illustrates the

maximum and minimum CARS experimental signal strengths of the pure rotational transitions for N_2, and it indicates that the system can be suppressed by a factor of approximately 6.

5.3 Raman polarizability tensor elements and effect of the non-resonant background

The CARSFT code previously utilized to obtain the theoretical simulation of N_2 spectra does not have the ability to model NO, and a spectral simulation has been developed to determine the pure rotational structure for the molecule nitric oxide. There are three essential constants used in a parametric study of their effects on the pure rotational transitions. It is important to note that all of these simulations were performed at room temperature, atmospheric pressure, a linewidth of 0.35 cm^{-1}, and parallel polarization.

The first constant is the polarizability tensor element $\langle \eta v | \hat{\alpha}_{q=2}^{k=2} | \eta v \rangle^2$ for NO, which is the element in the molecule-fixed reference frame that does not affect the rotational component of the wave equation. This can effectively be seen in Figure 5.8 where the rotational S branch transitions are relatively unaffected by the variation of the $\langle \eta v | \hat{\alpha}_{q=2}^{k=2} | \eta v \rangle^2$ parameter. Around 120 cm^{-1}, it becomes evident that an increase in this tensor element increases the strength of the electronic Raman transitions between the $^2\Pi_{1/2}$ and $^2\Pi_{3/2}$ ground electronic states. As the tensor element decreases, the electronic Raman transitions effectively have no influence in the baseline of the CARS signal.

The second constant is the anisotropy γ_0^2 for NO which is an invariant of the polarizability tensor. The expression for the anisotropy is given in the following equation where it is the sum of the spherical tensor elements.

$$\gamma_0^2 = \frac{3}{2} \sum_q \langle \eta v_A | \hat{\alpha}_q^2 | \eta v_A \rangle^2 \tag{5.15}$$

Figure 5.9 illustrates the effect of increasing and decreasing the anisotropy for NO, and the greatest influence it has is that it greatly affects the signal strength of the rotational transitions. As it decreases, the electronic Raman transitions dominate the signal around the 120 cm^{-1} features.

The third constant is the nonresonant CARS signal varied in Figure 5.10. The primary significance of the nonresonant signal is the baseline of the rotational spectrum. A larger value of the nonresonant constant resulted in an elevated baseline to the point where the small lift occurring at the 120 cm^{-1} features is no longer visible. A larger nonresonant constant also changed the bottom shape of the rotational signals between the $^2\Pi_{3/2}$ and $^2\Pi_{1/2}$ S branch transitions. Once the nonresonant signal was on the order of 10^{-14}, it appeared that it did not have any significant changes to the rotational spectrum of NO by further reduction in its value.

5.4 Dual-Pump CARS system analysis of nitric oxide

The spectrum for nitric oxide has been recorded by utilizing the dual-pump CARS system to determine the polarization effects on its pure rotational structure. Since the depolarization ratio of nitric oxide is unknown, it is assumed that NO exhibits a similar behavior to N_2 with regards to polarization. The gaseous mixture measured in the dual-pump CARS system was from the same source of 50 % NO and 50 % He used in the DBB-PRCARS experiment. The Stokes beam was placed at an angle of 62° with respect to both the pump and the probe beam while the analyzer was set to 0° for the data shown in Figure 5.11. The data almost exactly matched the NO spectrum analyzed by the DBB-PRCARS system in which the S branches dominate the pure rotational transitions. The analyzer was then set to -52° as shown in Figure 5.12, which was determined to be the best suppression of the S branches for nitrogen. As there was less CARS

signal as a result of the polarization suppression of the S branch, more energy had to be provided to the CARS system in order to obtain a higher signal-to-noise ratio. This increase in energy resulted in ionization of the nitric oxide molecule and a noticeable amount of noise occurring at wavenumbers less than 60 cm^{-1} in the Raman shift. While the ionization was undesirable for this experiment, Esherick and Owyoung [35] were able to use the ionization of NO to enhance the fundamental vibrational transition occurring at 1875 cm^{-1} in stimulated Raman spectroscopy. Nonetheless, the primary goal of polarization suppression of the dual-pump CARS system was intended to exhibit features occurring near the 120 cm^{-1} mark which appear unaffected by the ionization. Around 120 cm^{-1}, the Q branch transitions between the ground electronic states appear to have been influenced by the polarization scheme identically to the S branch transitions. If the Q branch transitions would have remained unsuppressed and dominated the pure rotational spectrum, then Figure 5.12 would have looked more closely to Figure 5.8 where the highest value of $\langle \eta v | \alpha_{q=2}^2 | \eta v \rangle^2$ resulted in an overactive Q branch.

With the information gained through this experiment, it is possible to use a spectral simulation designed for nitric oxide's pure rotational spectrum in order to determine species specific constants. The data depicted in Figure 5.11 has been normalized and compared with the normalized output of the spectral simulation for NO and is shown in Figure 5.13. This figure indicates that there is good agreement between the data and theory, which allowed for nitric oxide CARS measurements to be fit for application purposes of laser diagnostics in the future. The constants used to fit the data are: $\langle \eta v | \alpha_{q=2}^2 | \eta v \rangle^2 = 2.5 * 10^{-82} \left(\frac{C^4 m^2}{J^2}\right)$, $\gamma_o^2 = 10^{-80} \left(\frac{C^4 m^2}{J^2}\right)$, $\sigma_{nr} = 1.6 * 10^{-14} \left(\frac{m^2 C^2}{J^2}\right)$ and a spectral linewidth of 0.85.

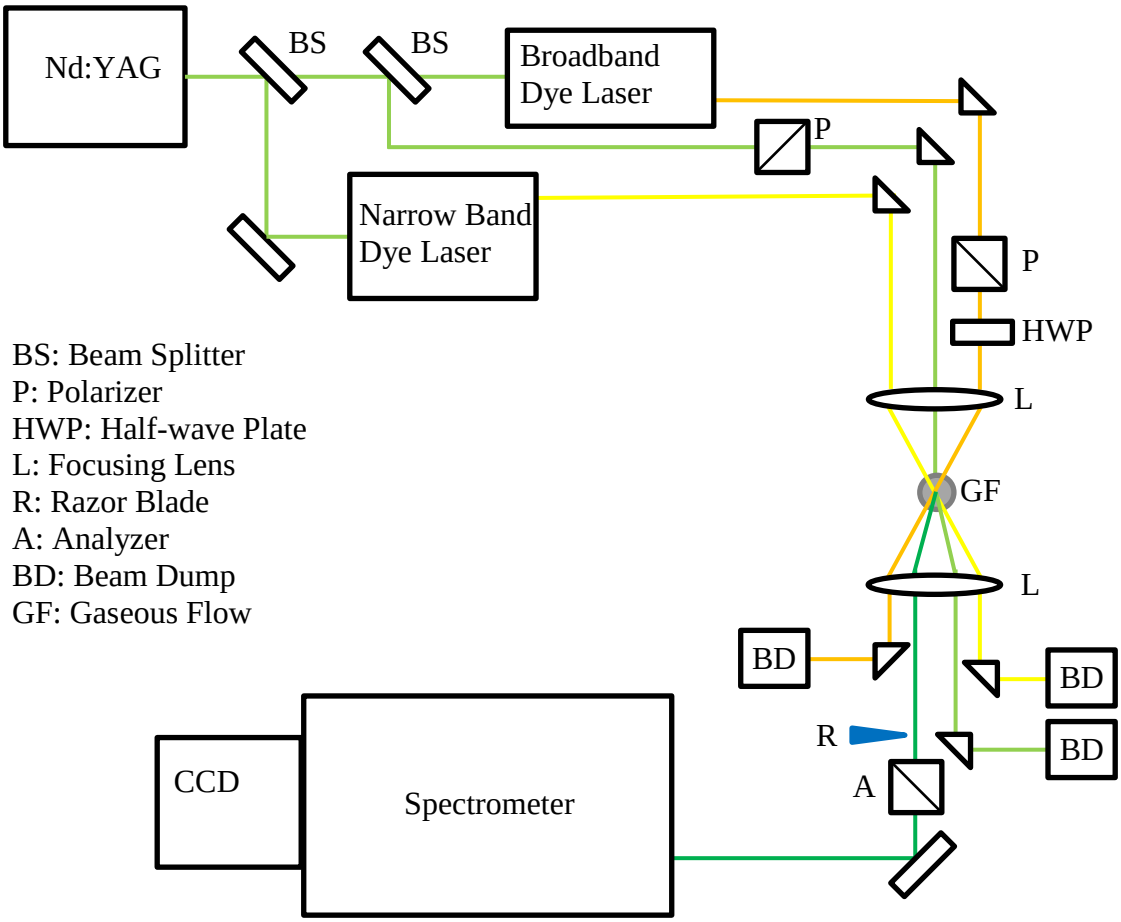

Figure 5.1: Dual-Pump Combined CARS System optical layout

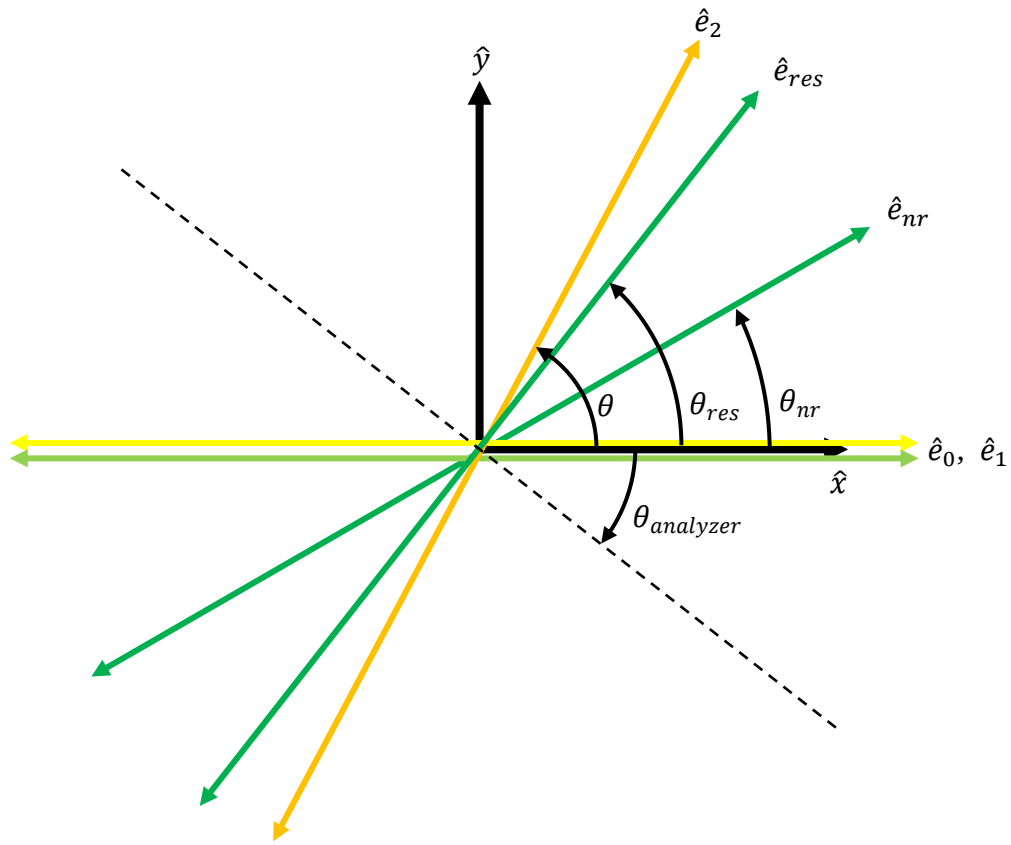

Figure 5.2: Polarization diagram of pump, probe, Stokes, and resonant CARS signal for polarization suppression of the rotational transitions of N_2

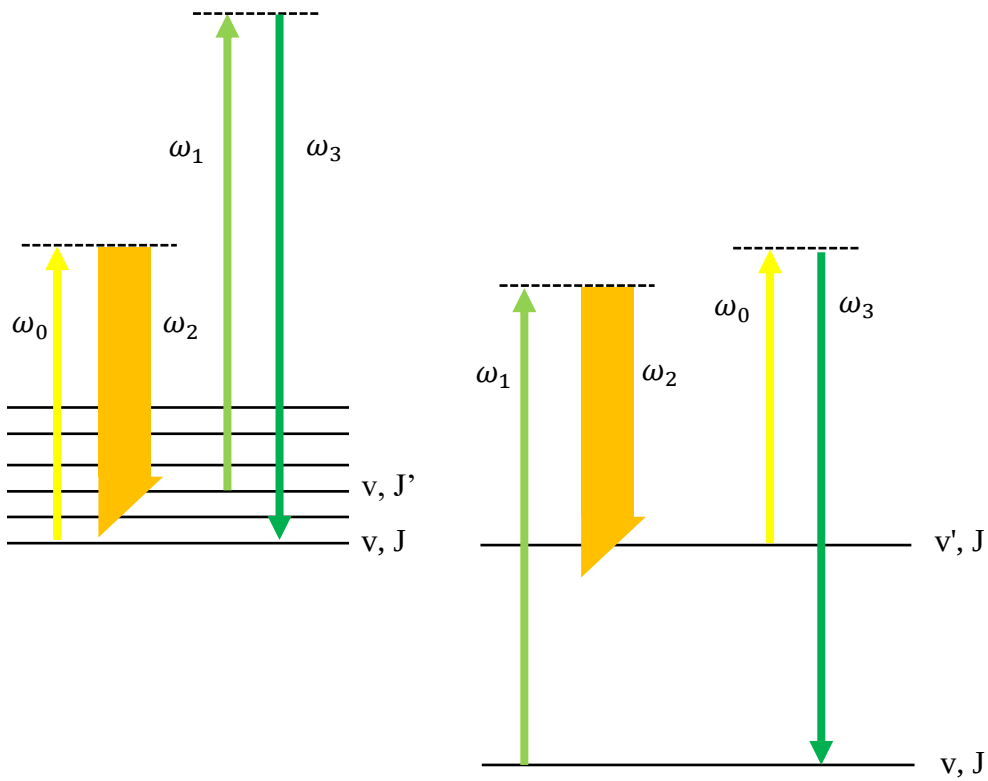

Figure 5.3: Energy level diagram for simultaneous acquisition of rotational and vibrational spectrum

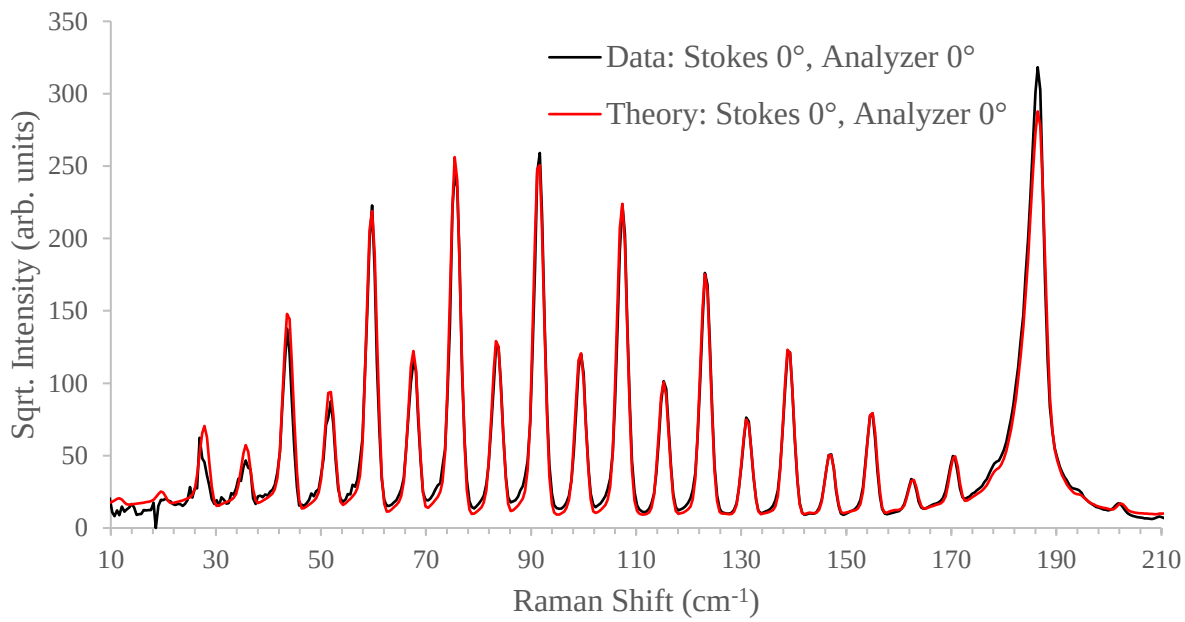

Figure 5.4: Comparison between experiment and theory from CARSFT code for simultaneous acquisition of vibrational and rotational branches of N_2

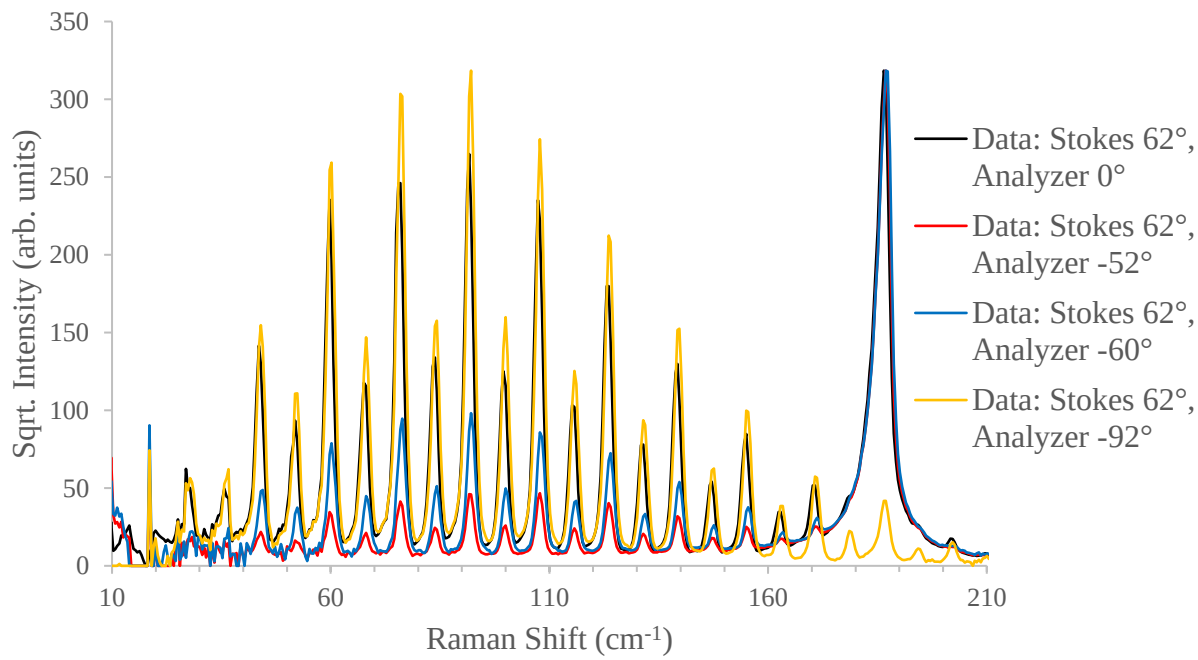

Figure 5.5: Polarization suppression of N_2 rotational and vibrational levels by keeping Stokes beam constant and varying analyzer angle experimental data

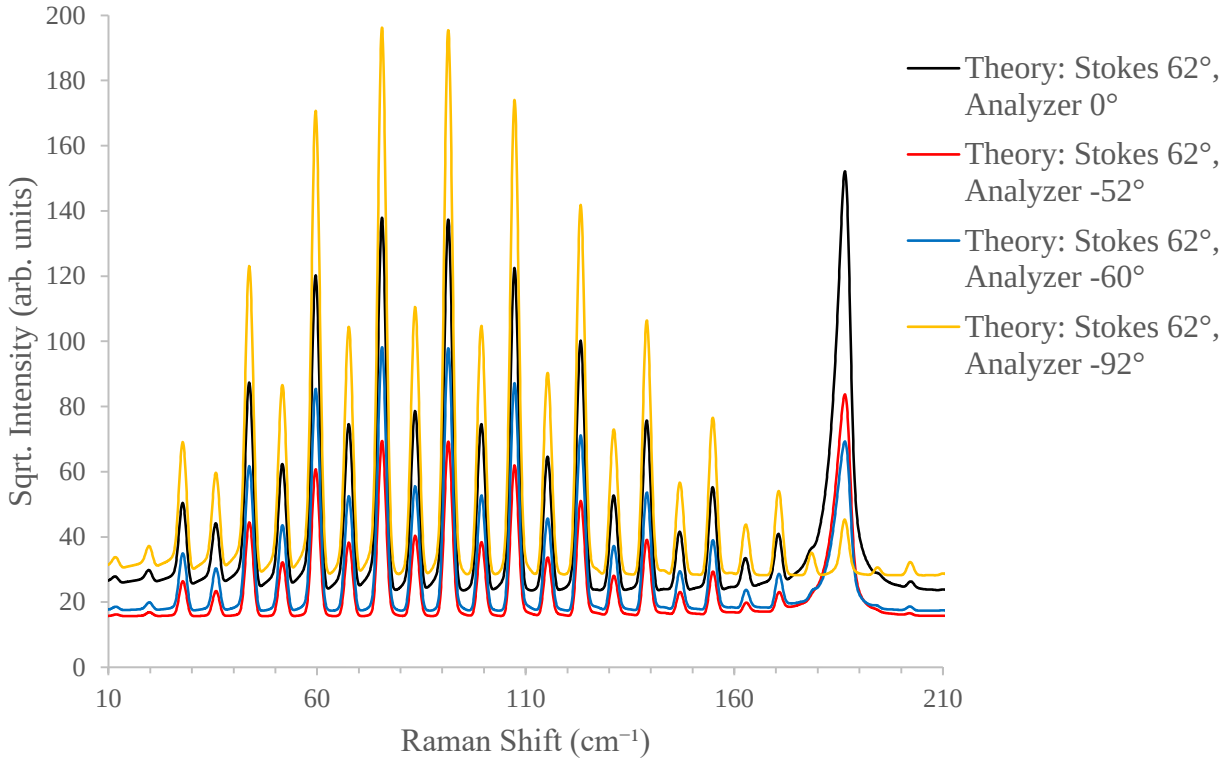

Figure 5.6: Polarization suppression of N_2 rotational and vibrational levels by keeping Stokes beam constant and varying analyzer angle CARSFT theory

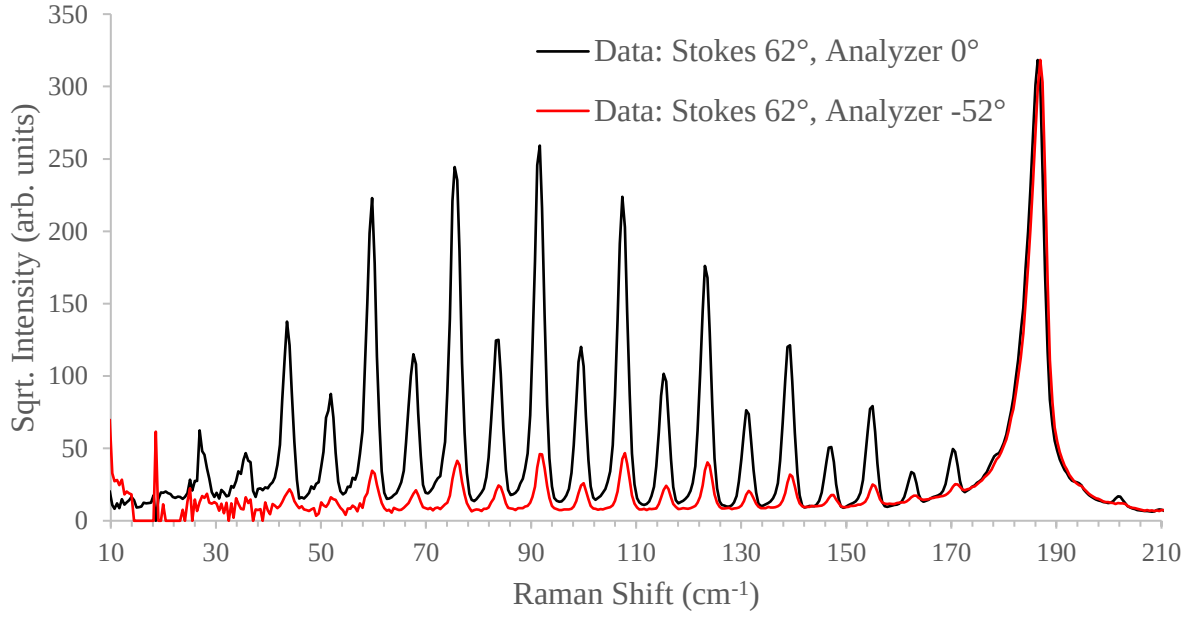

Figure 5.7: Polarization suppression of rotational S branch transitions of N_2

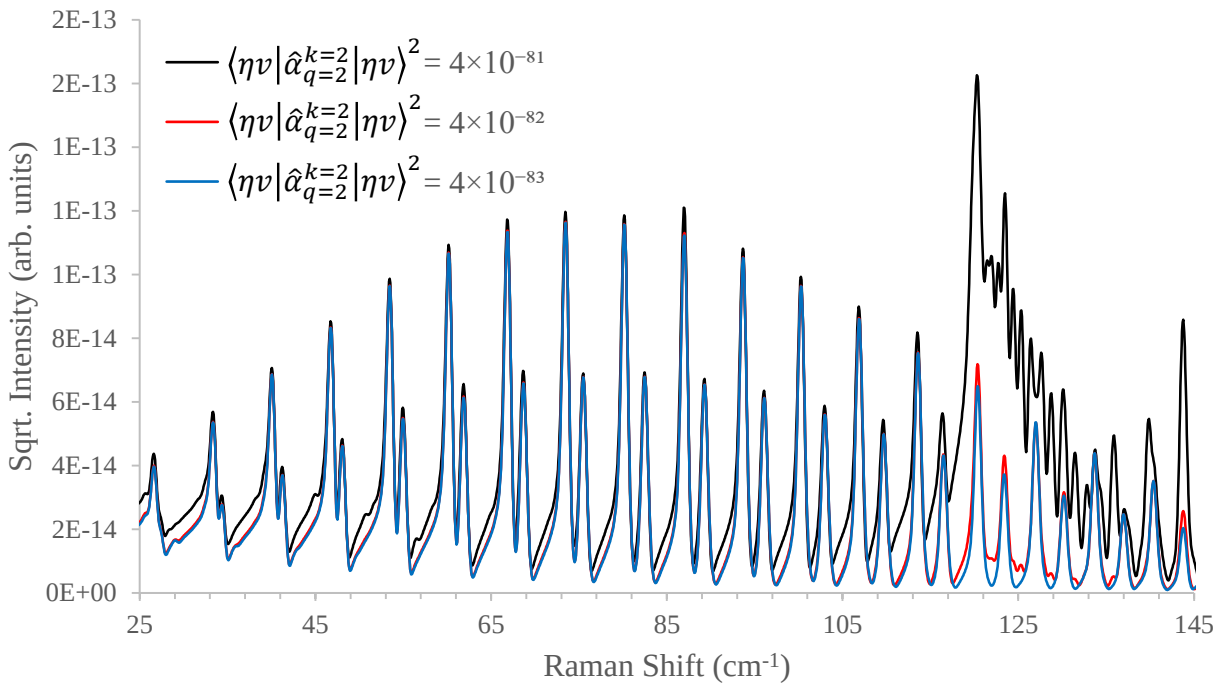

Figure 5.8: Variation of alpha term $\langle \eta v | \hat{\alpha}_{q=2}^{k=2} | \eta v \rangle^2$ in NO spectral simulation while holding all other terms constant

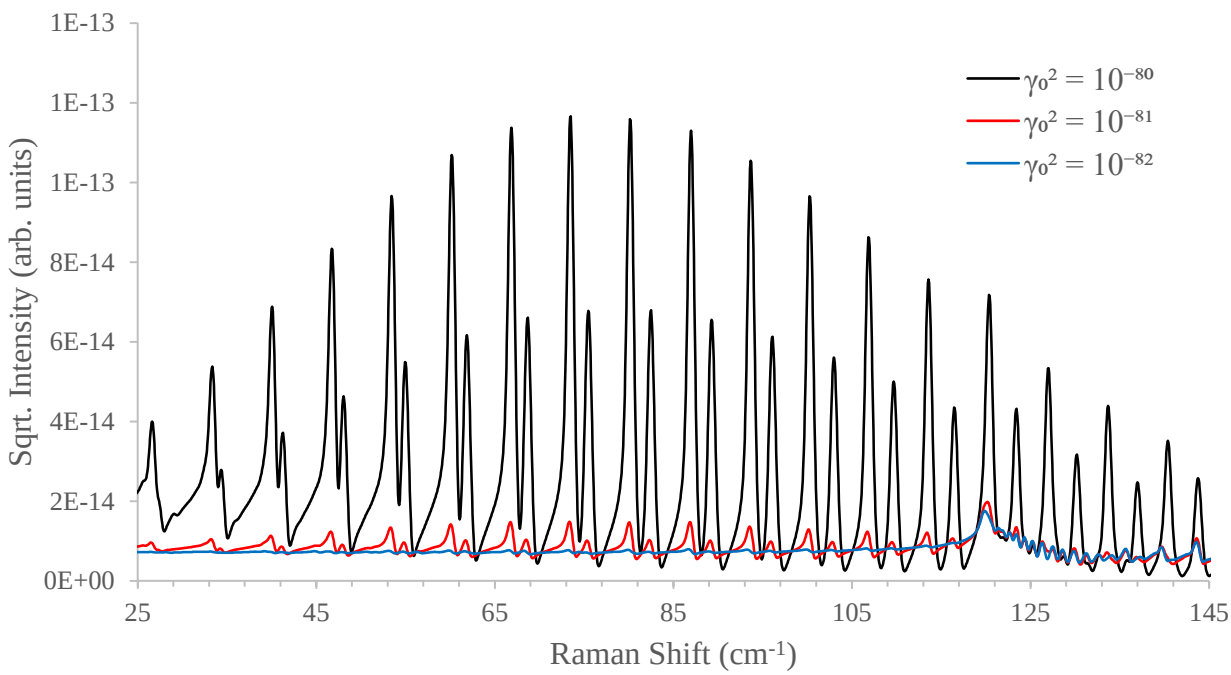

Figure 5.9: Variation of gamma term (γ_0^2) in NO spectral simulation while holding all other variables constant

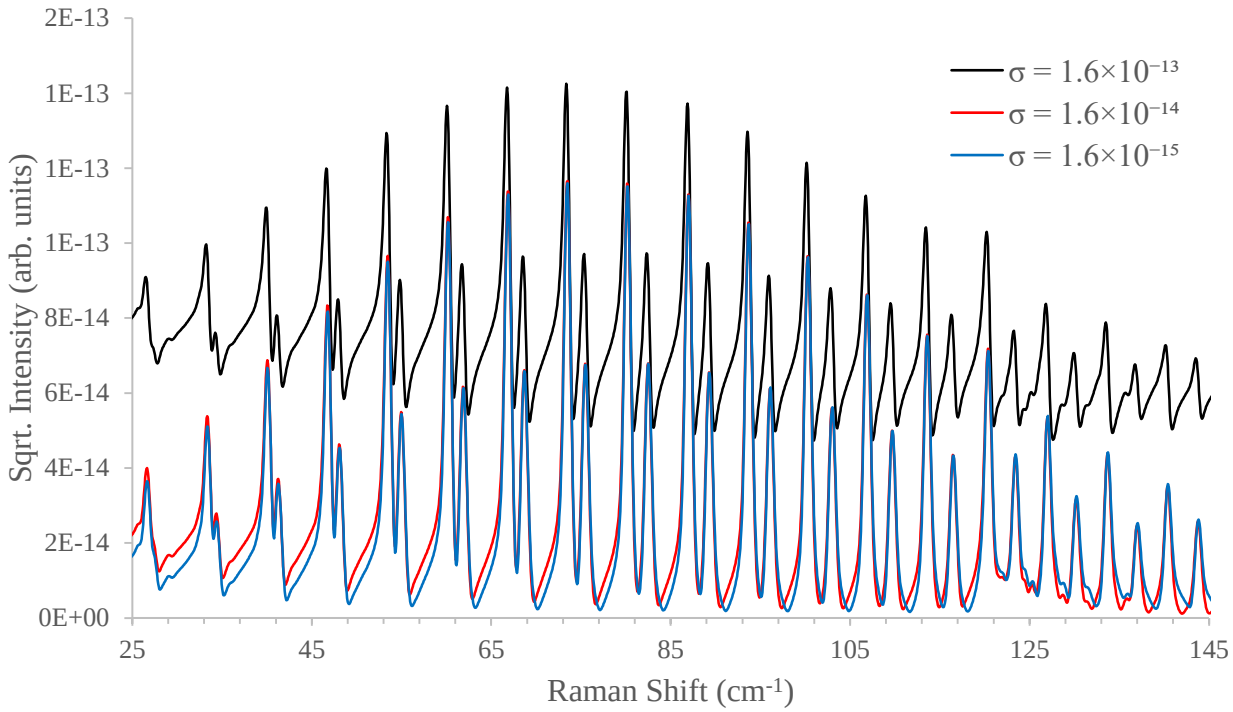

Figure 5.10: Variation of non-resonant term (σ) in NO spectral simulation while holding all other terms constant

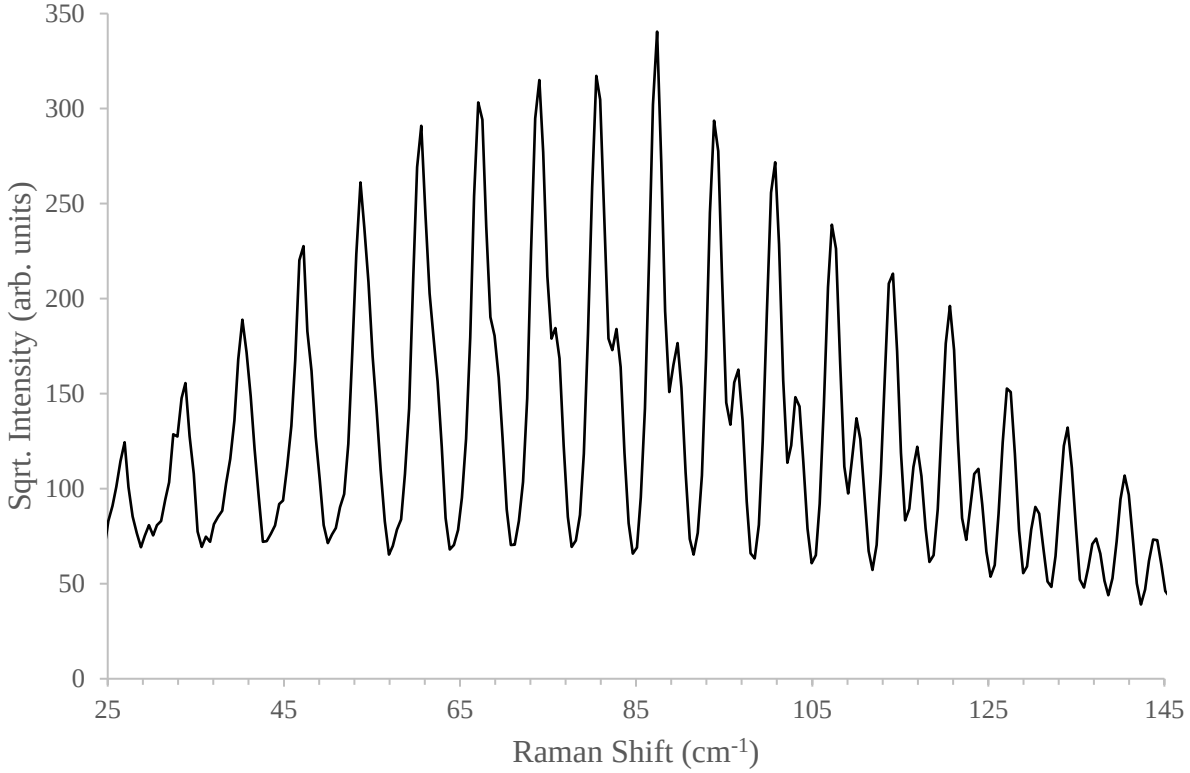

Figure 5.11: The rotational spectrum of NO with Stokes beam at 62° and the analyzer at 0°

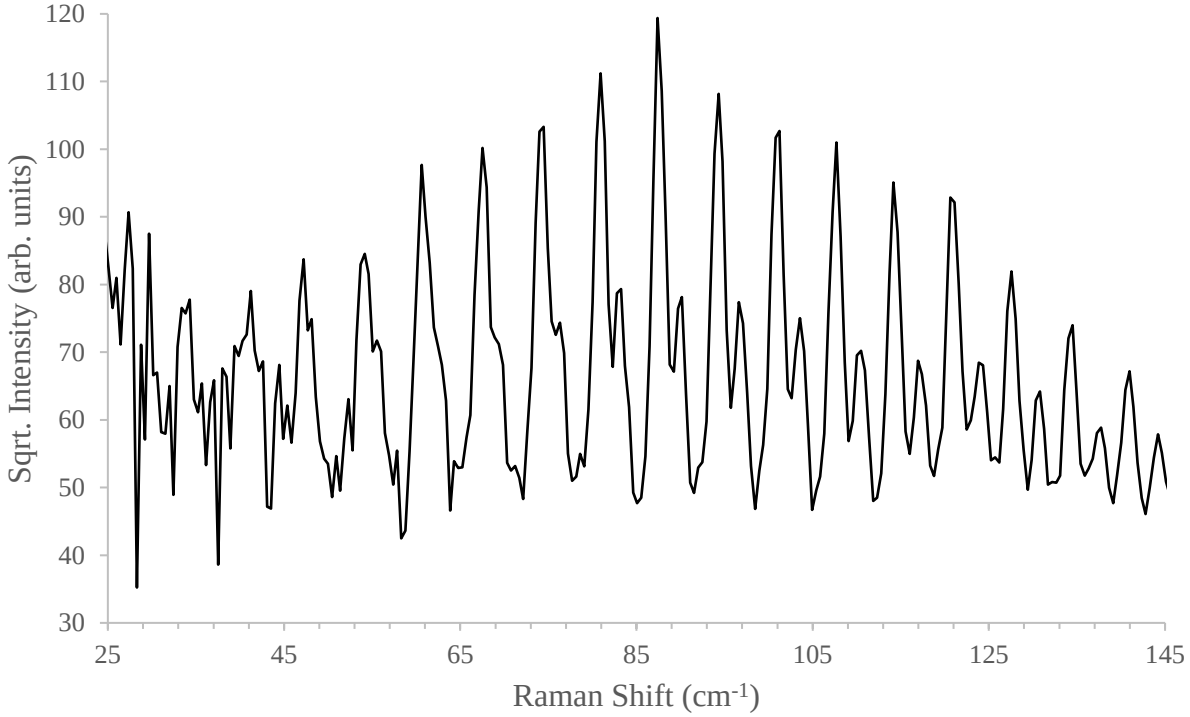

Figure 5.12: The rotational spectrum of NO with Stokes beam at 62° and the analyzer at -52°

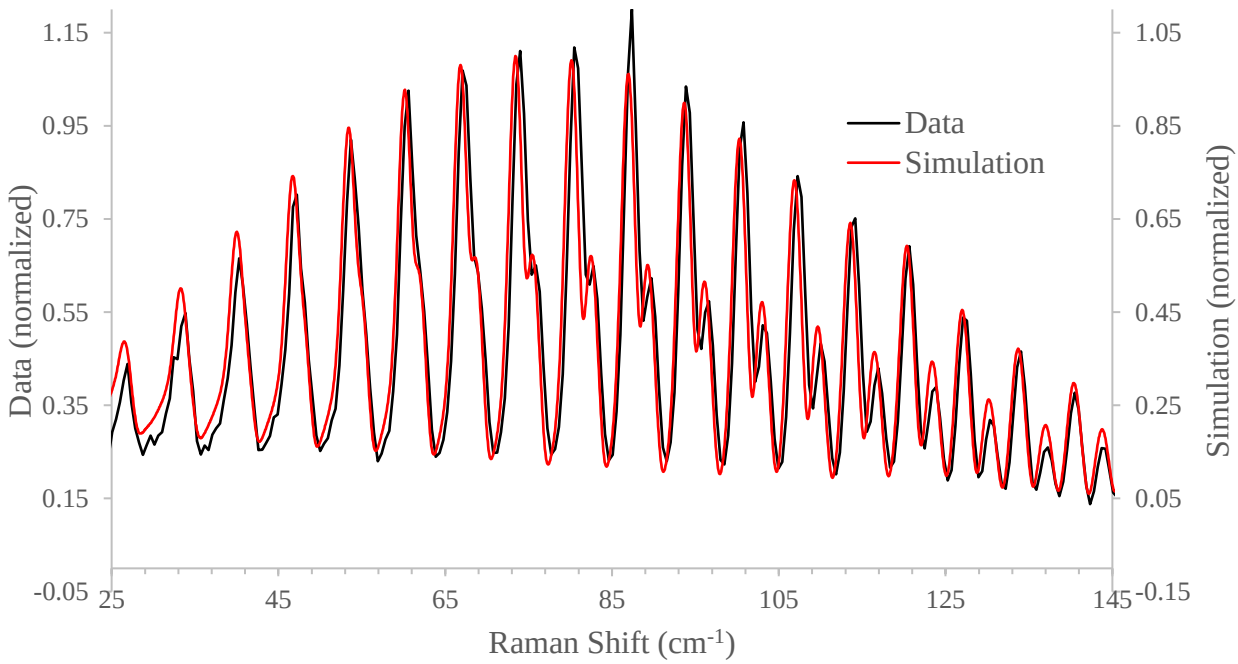

Figure 5.13: Comparison between NO spectral simulation and experimental results when the Stokes beam is 62° and the analyzer is 0°

6. CONCLUSIONS

6.1 Summary

A dual-broadband pure rotational coherent anti-Stokes Raman scattering experiment was performed to study the pure rotational structure of the nitric oxide molecule. The spectrum was observed at ambient temperature and atmospheric temperature in order to visualize a small lift in the baseline at 120 cm^{-1}, but it was not clearly evident in the experimental data. This feature has been presented in literature to be the electronic Raman transitions between the $^2\Pi_{1/2}$ and $^2\Pi_{3/2}$ energy levels. The resolution of the system was not capable of visualizing the R branch transitions that occur at a Raman shift less than 20 cm^1. This system was not adaptable for a polarization analysis of the pure rotational structure of nitric oxide since it is difficult to distinguish between the pump and Stokes laser beams.

A dual-pump coherent anti-Stokes Raman scattering experiment was performed to study the effect polarization exhibits on the pure rotational structure of nitric oxide. A theoretical calculation was performed and compared with the experimental polarization suppression of the rotational S branch transitions of nitrogen. It was assumed that the rotational levels of nitric oxide would behave in a similar manner as nitrogen, and a suppressed spectrum was displayed for both molecules. The key finding of this experiment was that the electronic transitions between the $^2\Pi_{1/2}$ and $^2\Pi_{3/2}$ ground electronic states behaves in a similar manner to the rotational S branch transitions when subjected to polarization suppression. The experimental data obtained was compared to a spectral simulation that has been developed by Dr. Lucht to understand the theoretical aspects of nitric oxide pure rotational transitions. There was good agreement between the experimental data and simulation for the unsuppressed case.

6.2 Future Work

While both the DBB-PRCARS and Dual-Pump CARS system have been able to clearly show the pure rotational S branch transitions and the effect of polarization on the Q branch transitions, neither system was able to accurately depict the structure of the R branch transitions for nitric oxide. These transitions occur below approximately 20 cm^{-1}, and there was not enough spectral dispersion around the Rayleigh line in order to resolve these transitions. The best method to exhibit the R branch transitions would be to decrease the overall linewidth of the experimental system such that each transition is discernable from the next. A camera lens can then be placed between the spectrometer and the CCD in order to increase the resolution of the Raman shifts. The experimental data, as a result of these modifications, would allow for the comparison with theoretical calculations of the rotational R branch transitions of NO.

Another potential work that may be completed in the future is cooling nitric oxide down to as low as 100 Kelvin in order to observe changes in the spectrum. Figure 6.1 through Figure 6.3 illustrate what theoretically occurs to the spectrum at lower temperatures up to and below the boiling point of NO which occurs at 121 K. For temperatures below the boiling point, NO becomes a liquid unless the pressure is decreased below atmospheric pressure. At lower temperatures, the lower S branch rotational levels become more populated than the upper levels as shown in Figure 6.1. It appears that the difference in relative intensity between the $^2\Pi_{1/2}$ and $^2\Pi_{3/2}$ for the rotational S branch transitions appears to grow at lower temperatures and is most easily observed in Figure 6.2. The electronic transitions between the two ground electronic states around 120 cm^{-1} also appears to remain constant as the temperature decreases, but the S branch rotational transitions appear to decrease in strength at lower temperatures in Figure 6.3.

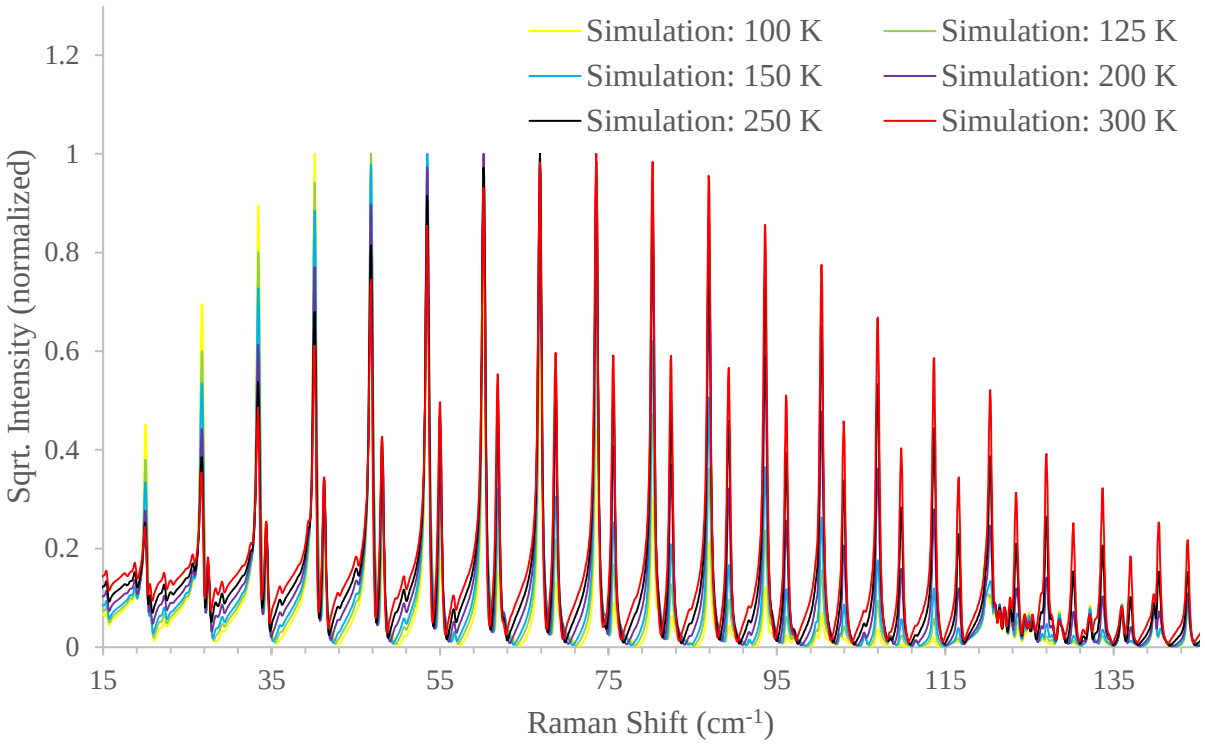

Figure 6.1: Spectral simulation of NO at varying temperatures from 100 K to 300 K

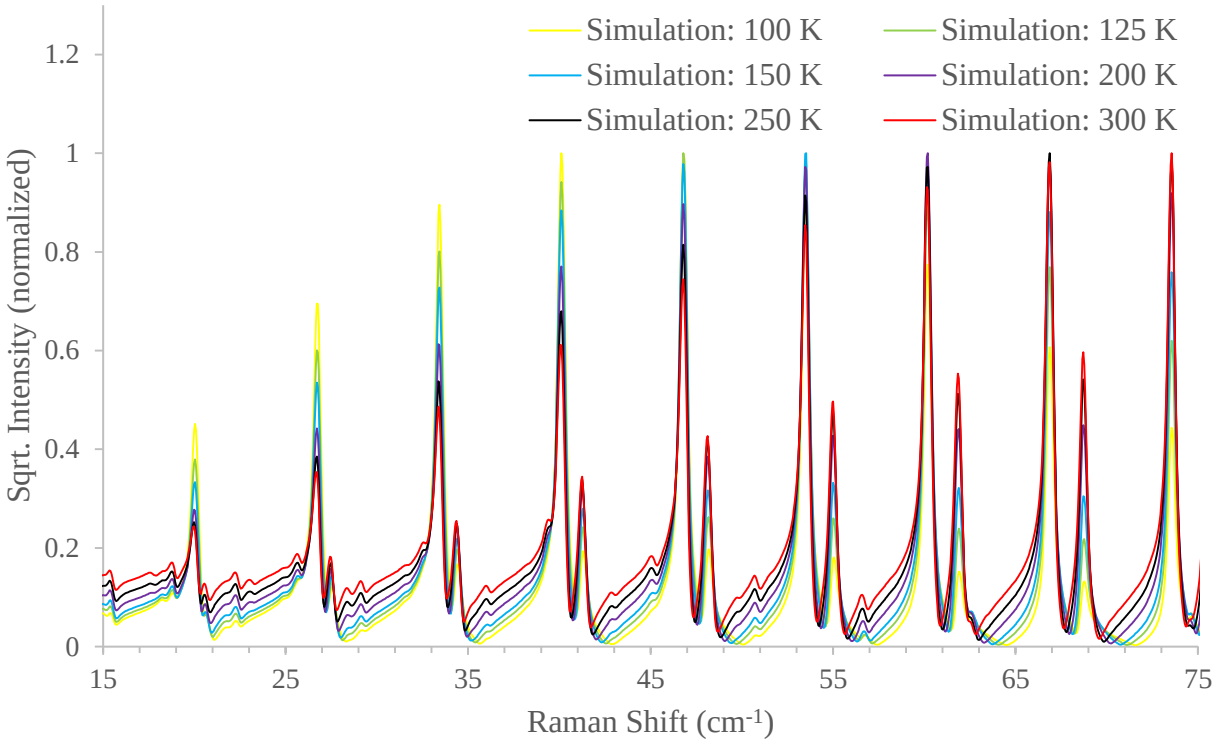

Figure 6.2: Closer look at lower J level S branch transitions of spectral simulation at varying temperatures from 100 K to 300 K

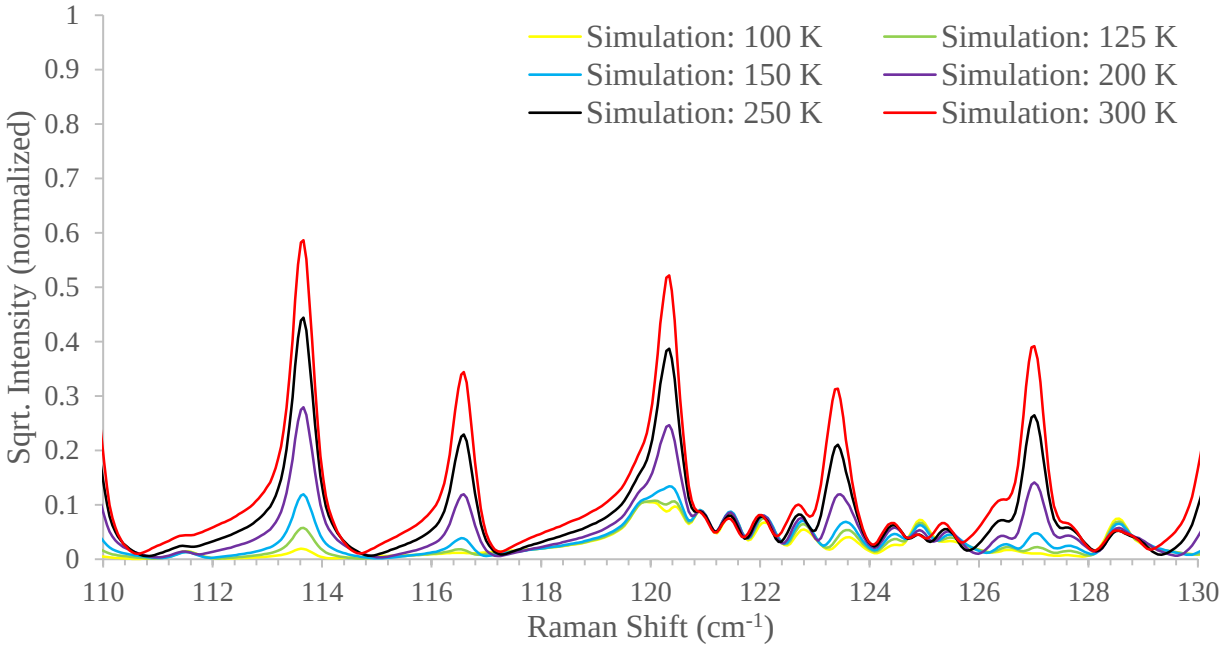

Figure 6.3: Closer look around the 120 cm^{-1} Q branch transitions of spectral simulation at varying temperatures from 100 K to 300 K

REFERENCES

[1] E. Culotta and D. E. Koshland, "NO News Is Good News," *Science,* vol. 258, no. 5090, pp. 1862-1865, 1992.

[2] R. P. Lucht, *ME 687: Laser Diagnostics for Reacting Flows class notes,* Purdue University, 2018.

[3] A. C. Eckbreth, Laser diagnostics for combustion temperature and species, Amsterdam, Netherlands: Gordon & Breach, 1996.

[4] A. Satija, "Development and Application of Coherent Anti-Stokes Raman Scattering Systems in Reacting Flows," Ph.D. Dissertation, School of Mechanical Engineering, Purdue University, West Lafayette, IN, 2013.

[5] A. C. Eckbreth, "BOXCARS: Crossed-beam phase-matched CARS generation in gases," *Applied Physics Letters,* vol. 32, no. 7, pp. 421-423, 1978.

[6] N. M. Laurendeau, Statistical Thermodynamics: Fundamentals and Applications, Cambridge University Press, 2005.

[7] R. P. Lucht, R. E. Palmer and M. A. Maris, "Simultaneous acquisition of pure rotational and vibrational nitrogen spectra using three-laser coherent anti-Stokes Raman spectroscopy," *Optics Letters,* vol. 12, no. 6, pp. 386-388, 1987.

[8] C. M. Penney, R. L. St Peters and M. Lapp, "Absolute rotational Raman cross sections for N2, O2, and CO2," *Journal of the Optical Society of America,* vol. 64, no. 5, pp. 712-716, 1974.

[9] F. Rasetti, "Über das Ramanspektrum des Stickoxyds," *Zeitschrift für Physik,* vol. 66, no. 9-10, pp. 646-649, 1930.

[10] D. L. Renschler, J. L. Hunt, T. K. McCubbin and S. R. Polo, "Rotational Raman Spectrum of Nitric Oxide," *Journal of Molecular Spectroscopy,* vol. 32, pp. 347-350, 1969.

[11] H. Fast, H. L. Welsh and D. W. Lepard, "Electronic Raman effect of nitric oxide at high resolution," *Canadian Journal of Physics,* vol. 47, pp. 2879-2881, 1969.

[12] D. W. Lepard, "Theoretical calculations of electronic Raman effects of the NO and O2 molecules," *Canadian Journal of Physics,* vol. 48, no. 14, pp. 1664-1674, 1970.

[13] A. Beckmann, H. Fietz, W. Kiefer and J. Laane, "Coherent anti-Stokes Raman-spectroscopy studies of nitric oxide," *Physical Review A,* vol. 24, no. 5, pp. 2518-2522, 1981.

[14] T. Doerk, J. Ehlbeck, R. Jedamzik, J. Uhlenbusch, J. Hoschele and J. Stienwandel, "Application of Coherent Anti-Stokes Raman Scattering (CARS) Technique to the Detection of NO," *Applied Spectroscopy,* vol. 51, no. 9, pp. 1360-1368, 1997.

[15] W. D. Kulatilaka, N. Chai, S. V. Naik, N. M. Laurendeau and R. P. Lucht, "Measurement of nitric oxide concentrations in flames by using electronic-resonance-enhanced coherent anti-Stokes Raman scattering," *Optics Letters,* vol. 31, no. 22, pp. 3357-3359, 2006.

[16] N. Chai, W. D. Kulatilaka, S. V. Naik, N. M. Laurendeau, R. P. Lucht, J. P. Kuehner, S. Roy, V. R. Katta and J. R. Gord, "Nitric oxide concentration measurements in atmospheric pressure flames using electronic-resonance-enhanced coherent anti-Stokes Raman scattering," *Applied Physics B,* vol. 88, no. 1, pp. 141-150, 2007.

[17] M. Alden, P.-E. Bengtsson, H. Edner, S. Kroll and D. Nilsson, "Rotational CARS: a comparison of different techniques with emphasis on accuracy in temperature determination," *Applied Optics,* vol. 28, no. 15, pp. 3206-3219, 1989.

[18] A. C. Eckbreth and T. J. Anderson, "Simultaneous rotational coherent anti-Stokes Raman spectroscopy and coherent Stokes Raman spectroscopy with arbitrary pump-Stokes spectral separation," *Optics Letters,* vol. 11, no. 8, pp. 496-498, 1986.

[19] J.-b. Zheng, J. B. Snow, D. V. Murphy, A. Leipertz, R. K. Chang and R. L. Farrow, "Experimental comparison of broadband rotational coherent anti-Stokes Raman scattering (CARS) and broadband vibrational CARS in a flame," *Optics Letters,* vol. 9, no. 8, pp. 341-343, 1984.

[20] M. Alden, P.-E. Bengtsson and H. Edner, "Rotational CARS generation through a multiple four-color interaction," *Applied Optics,* vol. 25, no. 23, pp. 4493-4500, 1986.

[21] A. Satija and R. P. Lucht, "Development of a combined pure rotational and vibrational coherent anti-Stokes Raman scattering," *Optics Letters,* pp. 1340-1342, 2013.

[22] A. C. Eckbreth and T. J. Anderson, "Dual broadband CARS for simultaneous, multiple species measurements," *Applied Optics,* vol. 24, no. 16, pp. 2731-2736, 1985.

[23] R. P. Lucht, "Three-laser coherent anti-Stokes Raman scattering measurements of two species," *Optics Letters,* vol. 12, no. 2, pp. 78-80, 1987.

[24] R. P. Lucht, V. Velur-Natarajan, C. D. Carter, K. D. Grinstead Jr., J. R. Gord, P. M. Danehy, G. J. Fiechtner and R. L. Farrow, "Dual-Pump Coherent Anti-Stokes Raman Scattering Temperature and CO2 Concentration Measurements," *AIAA Journal,* vol. 41, no. 4, pp. 679-686, 2003.

[25] S. Roy, T. R. Meyer, M. S. Brown, V. N. Velur, R. P. Lucht and J. R. Gord, "Triple-pump coherent anti-Stokes Raman scattering (CARS): temperature and multiple-species concentration measurements in reacting flows," *Optics Communications,* vol. 224, no. 1-3, pp. 131-137, 2003.

[26] S. Roy, T. R. Meyer, R. P. Lucht, M. Afzelius, P.-E. Bengtsson and J. R. Gord, "Dual-pump dual-broadband coherent anti-Stokes Raman scattering in reacting flows," *Optics Letters,* vol. 29, no. 16, pp. 1843-1845, 2004.

[27] R. N. Zare, Angular Momentum: Understanding Spatial Aspects in Chemistry and Physics, New York, NY: John Wiley and Sons, 1988.

[28] J. M. Brown and A. Carrington, Rotational Spectroscopy of Diatomic Molecules, Cambridge, United Kingdom: Cambridge University Press, 2003.

[29] A. R. Edmonds, Angular Momentum in Quantum Mechanics, Princeton, NJ: Princeton University Press, 1957.

[30] D. A. Long, The Raman Effect: A Unified Treatment of the Theory of Raman Scattering by Molecules, New York, NY: John Wiley and Sons, 2002.

[31] P. N. Butcher and D. Cotter, The Elements of Nonlinear Optics, Cambridge, United Kingdom: Cambridge University Press, 1990.

[32] M. D. Levenson and S. S. Kano, Introduction to Nonlinear Laser Spectroscopy: Revised Edition, London, United Kingdom: Academic Press, 1988.

[33] R. E. Palmer, "The CARSFT Computer Code for Calculating Coherent Anti-Stokes Raman Spectra: User and Programmer Information," Sandia National Lab., United States, 1989.

[34] A. Satija, M. T. Arendt, N. Chai and R. P. Lucht, "Dual-Broadband Coherent anti-Stokes Raman Scattering for Investigating Pure Rotational Raman Spectra of Nitric Oxide," AIAA SciTech 2019 Forum, 2019.

[35] P. Esherick and A. Owyoung, "Ionization-detected stimulated Raman spectroscopy," *Chemical Physics Letters*, vol. 103, no. 3, pp. 235-240, 1983.